

## Article

# Study and Modelling of the Impact of June 2015 Geomagnetic Storms on the Brazilian Ionosphere

Oladayo O. Afolabi <sup>1,2,\*</sup> , Claudia Maria Nicoli Candido <sup>2</sup>, Fabio Becker-Guedes <sup>2</sup> and Christine Amory-Mazaudier <sup>3</sup> 

- <sup>1</sup> National Space Research and Development Agency, Obasanjo Space Centre, Opp. Pyakasa Junction-KM 17 Airport Road, Garki, Abuja P.M.B. 437, Nigeria
- <sup>2</sup> Instituto Nacional De Pesquisas Espaciais, São Paulo 12227-010, BR, Brazil; claunicoli14@gmail.com (C.M.N.C.); fabio.guedes@inpe.br (F.B.-G.)
- <sup>3</sup> Laboratoire de Physique des Plasmas (LPP), Sorbonne Université, Ecole Polytechnique, Institut Polytechnique de Paris, Université Paris Saclay, Observatoire de Paris, CNRS, 75005 Paris, France; christine.amory@lpp.polytechnique.fr
- \* Correspondence: [afolabi.olayiwola@inpe.br](mailto:afolabi.olayiwola@inpe.br)

**Abstract:** This study investigated the impact of the June 2015 geomagnetic storms on the Brazilian equatorial and low-latitude ionosphere by analyzing various data sources, including solar wind parameters from the advanced compositional explorer satellite (ACE), global positioning satellite vertical total electron content (GPS-VTEC), geomagnetic data, and validation of the SAMI2 model-VTEC with GPS-VTEC. The effect of geomagnetic disturbances on the Brazilian longitudinal sector was examined by applying multiresolution analysis (MRA) of the maximum overlap discrete wavelet transform (MODWT) to isolate the diurnal component of the disturbance dynamo (*Ddyn*), DP2 current fluctuations from the ionospheric electric current disturbance (*Diono*), and semblance cross-correlation wavelet analysis for local phase comparison between the *Sq* and *Diono* currents. Our findings revealed that the significant fluctuations in DP2 at the Brazilian equatorial stations (Belem, dip lat:  $-0.47^\circ$  and Alta Floresta, dip lat:  $-3.75^\circ$ ) were influenced by IMF Bz oscillations; the equatorial electrojet also fluctuated in tandem with the DP2 currents, and dayside reconnection generated the field-aligned current that drove the DP2 current system. The short-lived positive ionospheric storm during the main phase on 22 June in the Southern Hemisphere in the Brazilian sector was caused by the interplay between the eastward prompt penetration of the magnetospheric convection electric field and the westward disturbance dynamo electric field. The negative ionospheric storms that occurred during the recovery phase from 23 to 29 June 2015, were attributed to the westward disturbance dynamo electric field, which caused the downward  $E \times B$  drift of the plasma to a lower height with a high recombination rate. The comparison between the SAMI2 model-VTEC and GPS-VTEC indicates that the SAMI2 model underestimated the VTEC within magnetic latitudes of  $-9^\circ$  to  $-24^\circ$  in the Brazilian longitudinal sector from 6 to 17 June 2015. However, it demonstrated satisfactory agreement with the GPS-VTEC within magnetic latitudes of  $-9^\circ$  to  $10^\circ$  from 8 to 15 June 2015. Conversely, the SAMI2 model overestimated the VTEC between  $\pm 10^\circ$  magnetic latitudes from 16 to 28 June 2015. The most substantial root mean square error (RMSE) values, notably 10.30 and 5.48 TECU, were recorded on 22 and 23 June 2015, coinciding with periods of intense geomagnetic disturbance.

**Keywords:** vertical total electron content (VTEC); prompt penetration of magnetospheric convection electric field; disturbance dynamo electric field (DDEF); DP2; Ddyn



**Citation:** Afolabi, O.O.; Candido, C.M.N.; Becker-Guedes, F.; Amory-Mazaudier, C. Study and Modelling of the Impact of June 2015 Geomagnetic Storms on the Brazilian Ionosphere. *Atmosphere* **2024**, *15*, 597. <https://doi.org/10.3390/atmos15050597>

Academic Editor: Yuichi Otsuka

Received: 10 December 2023

Revised: 1 January 2024

Accepted: 4 January 2024

Published: 14 May 2024



**Copyright:** © 2024 by the authors. Licensee MDPI, Basel, Switzerland. This article is an open access article distributed under the terms and conditions of the Creative Commons Attribution (CC BY) license (<https://creativecommons.org/licenses/by/4.0/>).

## 1. Introduction

The equatorial and low-latitude ionosphere ( $0^\circ$ – $30^\circ$  north and south of the Equator) is often a bubbling fountain of plasma that generates strong electron-density gradients. These gradients significantly disturb some types of communication and navigation signals

(e.g., GNSS, high-frequency radar systems) [1]. The equatorial ionosphere presents phenomena such as equatorial ionization anomaly (EIA), equatorial temperature and wind anomaly (ETWA), equatorial trough anomaly (ETA), equatorial plasma bubble, ionospheric scintillations, and equatorial spread F (ESF) [2–13].

During magnetic storms, two primary physical processes operating on a planetary scale can be observed: (1) the direct penetration of polar cap electric fields to the Equator, giving rise to the *DP2* current system [14–16], and (2) the disruption of winds caused by auroral joule heating and ion-drag acceleration, leading to the attenuation of the equatorial electrojet in the aftermath of the storm. Mayaud (1982) [17] initially formulated the theory of the direct penetration of polar cap electric fields to equatorial latitudes and predicted the shielding of the electric fields within 30 min [18,19]. Over the last three decades, numerous theoretical and experimental studies have focused on the direct penetration of polar cap electric fields into equatorial latitudes [20–23] and examined the thermospheric response to magnetic storms; subsequently, ref. [24] introduced the ionospheric disturbance dynamo to elucidate the electric field disturbance observed with the incoherent scatter sounder of Saint-Santin in the aftermath of the storm. This disturbance is attributed to the dynamo action of storm winds generated by auroral Joule heating [24–26].

The magnetospheric generator builds up excess positive charges on the dawn side of the magnetosphere and negative charges on the dusk side [27]. Charges with access to highly conducting magnetic field lines seek to relieve charge build-up by diverging from the source region. Current continuity requires that a divergence in the horizontal current be accompanied by a change in the field-aligned currents [27,28]. Magnetic merging immediately leads to field-aligned currents between the magnetosphere and ionosphere [29]. Region-1 (R1) currents are largely driven by magnetopause charge separation. These currents exist regardless of the direction of the interplanetary magnetic field [29,30]. When IMF  $B_z$  is southward, the R1 currents tend to be stronger, consistent with an enhanced merging electric field in the magnetotail. Another set of field-aligned currents, Region-2 (R2) currents, have their sources in the inner magnetosphere. Although their flow patterns are similar to those of the R1 currents, their polarity is opposite, and they intercept the ionosphere at a lower latitude. The R2 current system arises from a charge distribution that is a consequence of the drift of charged particles in Earth's dipole field [1,28,30–33].

Under equilibrium conditions with little or no convection, the magnetospheric particle gradient and curvature drift follow the contours of the magnetospheric electric potential  $\Phi$  [27,28,30]. When a cross-tail electric field  $E$  from convection enhancement develops, the plasmashet surges sunward, and a partial westward ring current develops. The dusk edge of the plasmashet is positively charged and the dawn edge is negatively charged. The excess charge creates a dusk-to-dawn polarization electric field. The superposition of the convection electric field and the polarization electric field tends to shield the near-Earth region from the enhanced dawn-to-dusk convection electric field. The shielding configuration usually prevents widespread surge of the electric field (known as prompt penetration of magnetospheric convection electric field PPMF) into the inner magnetosphere and low- and mid-latitude ionosphere [14,16,20,21,31,34].

However, the shielding layer and the field did not develop instantaneously. Thus, for short intervals, the inner magnetosphere and low- and mid-latitude ionosphere may be exposed to an enhanced convective electric field. This condition is known as undershielding [1,29–33]. Undershielding is the temporary penetration of the dawn-to-dusk electric field into the inner magnetosphere during the time of increasing convection [1]. During undershielding, the dusk-to-dawn polarization field (R2 region current) is insufficient to cancel the enhanced convective electric field [31]. A stronger convection field penetrates the field lines into the ionosphere (R1 region). On the other hand, when the driving convection field suddenly decreases as a result of a northward turning of the IMF  $B_z$ , the dusk-to-dawn polarization electric field dominates across the inner magnetosphere, which is referred to as overshielding. Overshielding is the temporary dominance of the dusk-to-dawn polarization field over the dawn-to-dusk convection field [1,19,31,32,35–39].

During the magnetically quiet period, the ionospheric regular dynamo gives rise to quiet solar ( $Sq$ ) and equatorial electrojet ( $EEJ$ ) current systems at middle and equatorial latitudes, respectively [32,40]. In contrast, during magnetically disturbed periods, intensified ionospheric electric currents known as auroral electrojets emerge in the auroral zone. These electrojets dissipate energy via the Joule heating effect, thereby influencing the temperature, pressure, and motion of the thermosphere. The perturbed thermospheric winds propagate toward mid- and low-latitudes, generating disturbed ionospheric electric fields, referred to as the disturbance dynamo electric field (DDEF), through the dynamo effect. Blanc and Richmond (1980) [24] introduced the first numerical simulation of an ionospheric disturbance dynamo.

This study focused on the magnetic manifestations of these physical processes on the equatorial electrojet ( $EEJ$ ) and global positioning satellite vertical total electron content (GPS-VTEC). Mazaudier (1985) [41] observed disturbance winds, a consequence of Joule heating, using incoherent scatter radar data, and their observations aligned with the predictions of the Blanc and Richmond model (1980) [24].

The geomagnetic storms of June 2015 have gained attention from numerous space scientists, such as [42–47]. Astafyeva et al. (2017, 2018) employed a multi-instrument to study the 22–23 June 2015 geomagnetic storms and observed the effect of eastward PPMEF, which caused short-lived positive ionospheric storms during the day, and the eastward DDEF caused long-lived positive ionospheric storms on the nightside of the main phase and the early stage of the recovery phase.

Mansilla et al. (2018) [47] also studied the same storm globally and observed increased total electron content (TEC) at high latitudes before the storm's main phase, significant asymmetry in TEC response between the middle and low latitudes of the Northern and Southern Hemispheres, and TEC decrease at equatorial latitudes. The prolonged TEC enhancements closely correlated with an increase in the  $O/N_2$  ratio; however, TEC decreases are not linked to reductions in the  $O/N_2$  ratio, unlike concurrent decrease in electron density. They concluded that eastward PPMEF significantly influenced the equatorial and low-latitude ionospheres during the main phase of the storm.

Paul (2018) examined the latitudinal ionospheric response during the three most prominent geomagnetic storms of 2015 during the solar cycles 24, 16–17 March 2015, 22–23 June 2015, and 19–22 December 2015 using TEC data derived from a latitudinal chain of GPS receivers that extend from  $70^\circ$  N to  $70^\circ$  S. They observed a symmetrical hemispheric response during the strongest 17 March (St. Patrick's Day) storm, and an asymmetric hemispheric response of the ionosphere during the 22 June and 20 December storms over the Asian-Australian sector and African equatorial and low-latitude sectors [46]. Amaechi (2018) examined the effects of the intense geomagnetic storms of 2015 on the occurrence of large-scale ionospheric irregularities over Africa and reported that irregularities occurred in the post-sunset to midnight period and are associated with TEC depletions and fluctuations due to equatorial plasma bubbles, which are stronger over the equatorial ionospheric anomaly (EIA) crest [48].

Singh (2017) investigated the impact of the 22–23 June 2015 geomagnetic storm on the Indian ionosphere by using ionosondes. They observed suppressed spread F during the westward penetration of the electric field of the overshielding R2 region in the Indian sector. Fluctuations in foF2 with shorter periods are attributed to eastward prompt penetration electric field fluctuations, whereas larger period fluctuations are mainly caused by disturbance wind, traveling ionospheric disturbances (TIDs), and DDEFs. In contrast to their detection in the European sector, plasma bubbles are suppressed in the Indian sector [29]. Macho (2020) studied ionospheric dynamics in the South American sector from 21 to 24 June 2015. They used ground ionosonde stations, GNSS receivers, very low-frequency (VLF), and magnetometer data. This study revealed an expansion of the crest of the equatorial ionospheric anomaly (EIA) at mid and high latitudes, mainly due to the prompt penetration of the electric field during the main phase [45].

In this study, we investigated the development of  $D_{dyn}$  in the Brazilian equatorial ionosphere in relation to auroral electrojet intensification due to the interaction between solar winds and the magnetosphere, the response of the equatorial electrojet to  $DP2$  fluctuations, and the westward  $D_{dyn}$  in the Brazilian sector during the main and recovery phases of geomagnetic storms in June 2015. We examined the impact of the *Diono* current on day-to-day VTEC redistribution and compared the SAMI2 model-VTEC with the GPS-VTEC for the days investigated in this study.

We introduced a novel approach by separating  $DP2$  fluctuations and  $D_{dyn}$  from the *Diono* current using two innovative techniques. The noteworthy aspect is the inaugural use of multi-resolution analysis of the maximum overlap discrete wavelet transform (MODWT) and semblance cross-correlation wavelet analysis for a detailed exploration of geomagnetic disturbances in Brazilian sector. This paper presents the first study of ionospheric signatures of space weather events in the Brazilian sector over a period of one month. Previous studies have generally focused on individual events. A similar study was conducted in the Indian sector recently [46].

The first section of this research work introduces and emphasizes the research gap that this article fills in the Brazilian sector. The second section presents the data sources and methodology. In the third section, we present the results of this study, and in the fourth section, we discuss and summarize the final results.

## 2. Data Source, Data Processing, and Model

### 2.1. Data Source

High-resolution interplanetary parameters in geocentric solar magnetospheric coordinates (GSM) recorded onboard the advanced composition explorer (ACE) satellite are being used to monitor the solar wind conditions. These are the solar wind speed ( $V_{sw}$ ), z-component of the interplanetary magnetic field (IMF  $B_z$ ), y-component of the interplanetary electric field (IEyF), and auroral electrojet indices (auroral upper boundary (AU) and auroral lower boundary (AL)). The data are made available by OMNIWeb data services via [http://omniweb.gsfc.nasa.gov/form/omni\\_min.html](http://omniweb.gsfc.nasa.gov/form/omni_min.html). This website was accessed on 28 August 2023.

Equatorial and low-latitude ionosphere responses to magnetic perturbation were examined by using the global navigation satellite system (GNSS-TEC) obtained by processing GNSS-RINEX files made available by the Brazilian Network for Continuous Monitoring of the GNSS System (RBMC) via <http://www.ibge.gov.br> (accessed on 28 August 2023). A map of the geographic coordinates of the GNSS receivers' stations are shown in Figure 1.

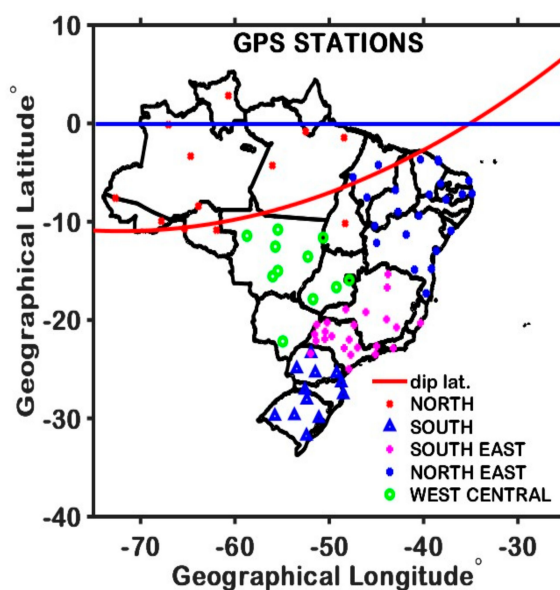


Figure 1. Map of GNSS receivers' stations.

The magnetic data used in this study were obtained from the Study and Monitoring of Brazilian Space Weather (EMBRACE) via <http://climaespacial/portal> and the South American Meridian B-Field Array (SAMBA) through <http://magnetometers.bc.edu> (both accessed on 23 August 2023). Magnetometers were installed in Belem (BELE:  $-1.41^\circ$ ,  $-48.18$ , dip lat:  $-0.47^\circ$ ), Cuiaba (CUIB:  $-15.55^\circ$ ,  $-56^\circ$ , dip lat:  $-8.71^\circ$ , and Alta Floresta (ALF:  $-9.87^\circ$ ,  $-56.10^\circ$ , dip lat:  $-3.74^\circ$ ), respectively. These magnetometers provided 1 min data resolution for the northward (X), eastward (Y), and vertical (Z) components of Earth's magnetic field. The geographic coordinates of the magnetometers' stations are shown in Figure 2.

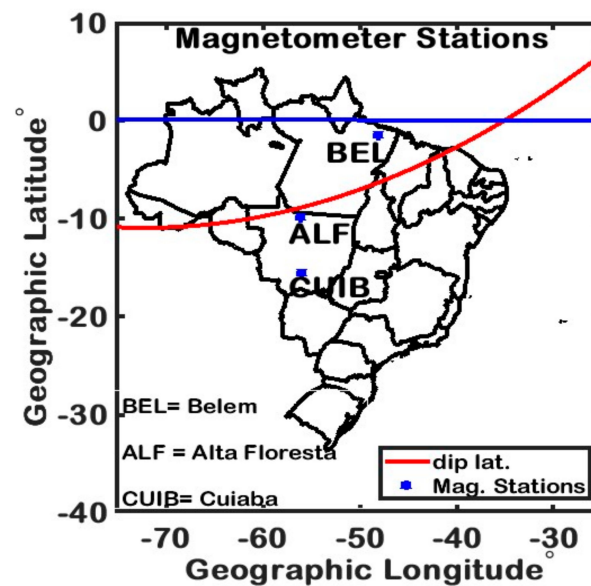


Figure 2. Map of magnetometer stations.

## 2.2. Data Processing

### 2.2.1. GPS Data

The GPS Receiver Independent Exchange Format (RINEX) files obtained from the Brazilian Network for Continuous Monitoring of GNSS Systems were processed by using GPS-TEC analysis application software developed by Gopi Seemala and Boston College, United States. Details of the GPS-TEC application software can be found in Seemala (2011) [49].

We computed the TEC-MAP using one-minute VTEC resolution data. The VTEC data were grid  $1^\circ \times 1^\circ$  in geographical latitude and longitude. The dip latitudes were computed using the British Geological Survey website ([https://geomag.bgs.ac.uk/cgi-bin/coord\\_calc](https://geomag.bgs.ac.uk/cgi-bin/coord_calc) (last accessed on 28 August 2023)). Magnetically quiet days were obtained from the International Service of Geomagnetic Indices (ISGI, <http://isgi.unistra.fr> (last accessed on 28 August 2023)). We computed the storm-time residual VTEC by subtracting the average VTEC of five magnetically quiet days from that of magnetically disturbed days.

$$Q_{5AVR} = \frac{1}{N} \sum_{1}^N MQD \quad (1)$$

$$\Delta TEC = MDs - Q_{5AVR} \quad (2)$$

Equations (1) and (2) expressed the mathematical computation processes for calculating the change in VTEC ( $\Delta VTEC$ ), where  $N$  denotes the number of magnetically quiet days,  $Q_{5AVR}$  is the average of five magnetically quiet days, and  $MDs$  is the magnetically disturbed days.

### 2.2.2. Computation of Equatorial Electrojet (EEJ)

$$H = \sqrt{X^2 + Y^2} \quad (3)$$

We computed the horizontal component of Earth's magnetic field from the X and Y components of Earth's magnetic field, as shown in Equation (3).

$$H_0 = \frac{H_{23} + H_{24} + H_{01} + H_{02}}{4}, \quad (4)$$

$$\delta H = H(t) - H_0 \quad (5)$$

To eliminate variations in offset values among different magnetometers, we first calculated the nighttime baseline values for the  $H$  component using Equation (4) for each day. These baseline values were then subtracted from the corresponding magnetometer dataset to obtain the hourly departure of  $H$ , which is denoted as  $\delta H$  and can be expressed using Equation (5). The baseline value is defined as the average of the  $H$  component nighttime (23:00–02:00 LT) values of Earth's magnetic field.

$H_{23}$ ,  $H_{24}$ ,  $H_{01}$ , and  $H_{02}$  are the hourly values of  $H$  at 23:00, 24:00, 01:00, and 02:00 in local time (LT).

$$\Delta c = \frac{\delta H_{01} - \delta H_{24}}{23} \quad (6)$$

The time variable  $t$  represents the hours ranging from 01:00 to 24:00 LT. The hourly departure,  $\delta H$ , was then adjusted for non-cyclic variation using Equation (6). This correction method was previously proposed by Rastogi et al. (2004), who defined noncyclic variation as a phenomenon where the value at 01:00 LT differs from that at local midnight (24:00 LT) [50].

$$S_q(t) = \delta H(t) + (t - 1) \cdot \Delta c \quad (7)$$

where  $t = 1$  to 1440.

The values for the solar quiet variation ( $S_q$ ) can be obtained by correcting the hourly departure of  $H$  ( $\delta H$ ) for the noncyclic variation based on the magnetometer dataset. This relationship is expressed by Equation (7).

$$\Delta H = H_{BELEM} - H_{CUIABA} \quad (8)$$

By selecting a station inside the  $EEJ$  current (Belem dip altitude:  $-0.47$ ) and a station outside the  $EEJ$  current (Cuiaba dip latitude:  $-8.71$ ), as shown in Equation (8), we determine the equatorial electrojet ( $EEJ$ ) [5,51,52].

$$V_d = 12.26 - 0.0454F10.7 + 0.1892\Delta H + 0.00028\Delta H^2 - 0.0000022\Delta H^3 \quad (9)$$

To estimate the vertical drift velocity from the ground-based magnetometer for day-time plasma drift, as given in Equation (9) [34,35], we used multiple regression analysis techniques, as suggested by Anderson (2004).

### 2.2.3. Computation of Ionospheric Electric Current Disturbance (Diono)

$$Diono = H - H_0 - S_R^H - SYMH \cdot \cos \varnothing \quad (10)$$

$$Diono = DP2 + Ddyn \quad (11)$$

The ionospheric electric current disturbance ( $Diono$ ) was computed by using Equation (10).  $Diono$  is the magnetic disturbance caused by the ionospheric electric current system [53–58].  $H$  is the Earth's horizontal magnetic field measured component,  $\varnothing$  is the magnetic latitude of the stations, and  $S_R^H$  is the daily regular fluctuation of  $H$  caused by the solar quiet ( $S_q$ ) system.  $S_R^H$  was calculated by averaging five magnetically quiet days provided by the World

Data Center Kyoto for Geomagnetism (Kyoto-u.ac.jp). *DP2* is the total magnetic disturbance related to the disturbance polar number 2 (*DP2*) fluctuations during the prompt penetration of the magnetospheric convection electric field (PPMEF), and *Ddyn* is the magnetic signature of the ionospheric disturbance dynamo caused by Joule heating in the auroral zone (Blanc and Richmond 1980) [24]. Joule heating generates disturbed thermospheric winds, which alter the quiet-time global thermospheric circulation. In this study, we refer to *Ddyn* as the magnetic signature of the ionospheric disturbance dynamo, first described by Le Huy and Amory-Mazaudier (2005, 2008) [40,59] as shown in Equation (11), ref. [15,16,55,56,60].

The ionospheric electric current disturbance (*Diono*) is the sum of *DP2* and *Ddyn*. We focused on the impact of *DP2* current fluctuations and *Ddyn* on the Brazilian equatorial and low-latitude ionosphere during geomagnetic storms in June 2015. Two techniques were used to isolate the effects of *DP2* and *Ddyn* on the Brazilian equatorial ionosphere. These techniques are:

- i. Multiresolution analysis (MRA) of maximum overlap discrete wavelet transforms (MODWT). We extracted the diurnal component of *Ddyn*, which had a period of approximately 24 h. For *DP2* current fluctuations, we extracted the *Diono* component, which has a period of less than 3 h [61–63].
- ii. Semblance cross-correlation wavelet analysis [54,64]. Interested readers can refer to the article published by Younas (2021) [54,64,65]. We performed a semblance analysis by comparing the local phase between the *Sq* and the *Diono* currents as a function of time and wavelength. The details of this new method to isolates *anti-Sq* from *Diono* can be found in [54]. The positive phase is represented by +1 and the negative phase is represented by −1 (which is *anti-Sq* current).

#### 2.2.4. Computation of Akasofu’s Parameter

When the interaction between the solar wind and magnetosphere intensifies, powerful magnetospheric currents are generated, and the magnetic energy density within the magnetosphere increases. This energy leads to the reconfiguration of the magnetosphere, faster movement of plasma in the plasmasheet, heating and acceleration of particles, and amplification of currents [66,67]. The movement of solar wind particles on Earth generates kinetic energy flux. The energy flux in the plasma plays a crucial role in shaping the magnetosphere. Additionally, the interplanetary magnetic field influences the magnetosphere through a flux known as the Poynting flux [1,67].

$$P = [(1/\mu_0)(E_{SW} \times B_{SW})](\sin(\theta/2))^4 = (1/\mu_0)v_{SW}|B_t|^2(\sin(\theta/2))^4 \tag{12}$$

where

$$P = \text{effective solar wind poynting flux } [W/m^2]$$

$$\mu_0 = \text{permeability of free space } \left(1.26 \times 10^{-6} \frac{N}{A^2}\right)$$

$$v_{SW} = \text{solar wind velocity } [m/s]$$

$$|B_t| = \text{magnitude of the tangential component of the IMF} = \sqrt{B_y^2 + B_z^2} [T]$$

$$\theta = \text{IMF polar angle in the Y-Z GSE plane } (\tan^{-1}(B_y/B_z)) [\text{deg or rad}]$$

$$\varepsilon = (1/\mu_0)v_{SW}|B_t|^2(\sin(\theta/2))^4 l^2 \tag{13}$$

The Poynting flux is the power delivered by electromagnetic sources. Akasofu (1981) estimated an electromagnetic power flux that represents the solar wind power delivered by magnetic merging, as shown in Equation (12). He assumed that only the tangential component *B<sub>t</sub>* of the IMF delivered energy; therefore, the *B<sub>x</sub>* component did not play a role. The elements in the square brackets of Equation (12) constitute the Poynting flux. The

factor outside the bracket accounts for the efficiency of energy entry by the anti-parallel component of the IMF.

For many storm-time applications, space weather scientists are most interested in the power delivered to the cross-section of the dayside magnetosphere. One version of power estimates the Akasofu epsilon parameter ( $\epsilon$ ), which is obtained by multiplying the effective solar wind Poynting flux by a factor proportional to the cross-sectional area of the magnetopause that intercepts the solar wind, as shown in Equation (13).

where

$\epsilon$  = Akasofu epsilon parameter ( $W$ )

$l^2$  = effective cross-sectional area of the merging region  $\approx (7R_E)^2$

Scientists frequently use  $\epsilon$  as a reference point when analyzing the energy distribution in magnetic storms. Nevertheless, in the case of severe storms, this estimation may become inaccurate because of significant fluctuations in the cross-sectional area of the magnetopause or the influence of other factors that are not well understood and can affect the efficiency of the energy transfer [1,66,67].

### 2.3. SAMI2 Model

SAMI2 (another model for ionosphere) calculates the evolution of the ionosphere in the low- to mid-latitudes. SAMI2 considers the dynamic plasma and chemical changes of seven ion species ( $H^+$ ,  $He^+$ ,  $N^+$ ,  $O^+$ ,  $N_2^+$ ,  $NO^+$ , and  $O_2^+$ ) within an altitude range of 85 km to 20,000 km. This altitude range corresponds to a latitudinal span of  $\pm 62.5^\circ$  around the magnetic equator [68].

SAMI2 solves the ion continuity and momentum equations for all seven ion species. In addition, it solves the temperature equation for  $H^+$ ,  $He^+$ ,  $O^+$  and the electrons. The code models the plasma along Earth's geomagnetic field, spanning from one hemisphere to another. For this purpose, it utilizes an offset-tilted dipole field.

The code incorporates a modeled  $E \times B$  drift of the plasma, which represents the motion of the plasma owing to the interaction between the electric field ( $E$ ) and magnetic field ( $B$ ). It also considers the ion inertia in the ion momentum equation to account for the motion along the dipole field line.

SAMI2 employs a fixed, nonorthogonal grid, where one coordinate axis aligns with the geomagnetic field. The neutral species were characterized using the empirical models NRLMSISE00 and HWM14. These models provide information regarding a neutral atmosphere, which is essential for understanding the ionosphere's behavior [68,69].

The input parameters in the SAMI2 model are F10.7A (3 months average F10.7), the daily value of F10.7, the daily value of  $A_p$ , the year, and the day. The SAMI2 code is coupled with the NRLMSISE00, HWM14, and EUVAC models developed by Richards [70]. By default, it is assumed that the ionosphere's perpendicular vertical  $E \times B$  drift, which is influenced by the magnetic field, can be either sinusoidal or defined by the  $E \times B$  drift model [26].

The primary outputs of the SAMI2 model include ion density, ion temperature, ion velocity along the magnetic field, electron temperature, time step in local time, geographic latitude, geographic longitude, and altitude. The details of the SAMI2 model can be found in an article by Hubal et al. (2000) [68].

## 3. Results

### 3.1. Impact of June 2015 Geomagnetic Storms on Brazilian Ionosphere

#### 3.1.1. The State of the Interplanetary Medium from 6 to 30 June 2015

In Figure 3, the 1-min resolution data for the interplanetary parameters, including IMF  $B_z$  and  $IEyF$  (refer to Figure 3a–c), along with the solar wind speed ( $V_{sw}$ ; refer to Figure 3a), are presented. The aim is to examine the concurrent patterns of auroral activity, achieved by comparing 1-min resolution auroral electrojet indices (refer to Figure 3d). These indices were derived from a network of strategically positioned ground-based magnetometers at latitudes where auroras are commonly observed. The AU index (highlighted in red)

signifies the envelope of the maximum northward disturbance recorded at all the stations, indicating an eastward auroral electrojet. Conversely, the AL index (depicted in black) represents the envelope of the minimum disturbance (maximum negative value) typically associated with the westward auroral electrojet. These indices offer a comprehensive overview of the auroral activity and prevailing electrojet conditions [71].

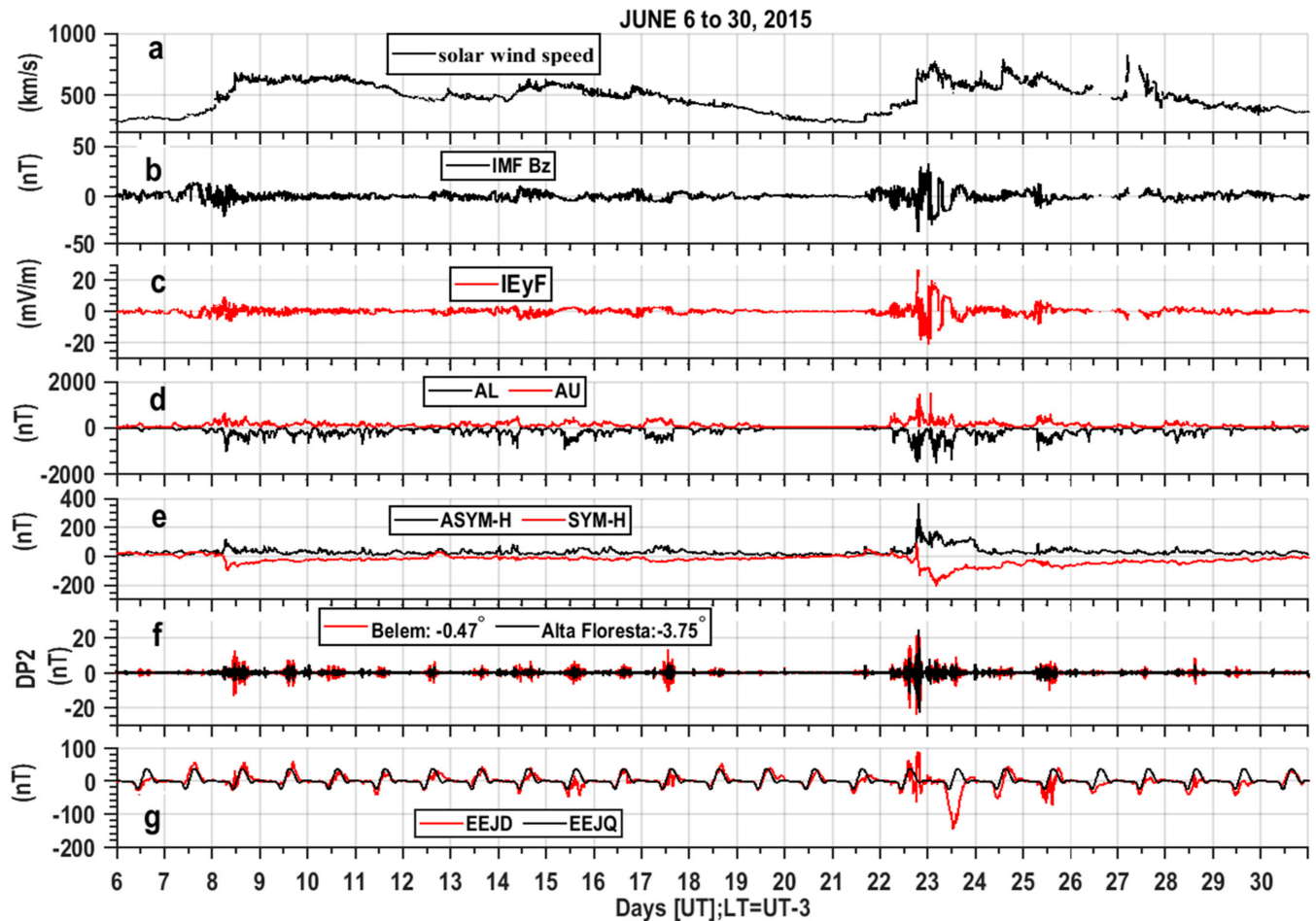


**Figure 3.** State of the interplanetary medium from 6 to 30 June 2015. (a) Velocity of the solar wind ( $V_{sw}$ ). In addition, (b) shows the IMF  $B_z$  (interplanetary magnetic field in the Z direction), (c) presents the y-component of interplanetary electric field, (d) portrays the aurora electrojet (AL: aurora lower boundary, AU: aurora upper boundary), (e) demonstrates the H-component symmetry of Earth's magnetic field observed at various low latitudes, and (f) illustrates  $DP2$  currents in Belem (dip lat:  $-0.47^\circ$ ) and Alta Floresta ( $-3.75^\circ$ ). Further, (g) shows the day-to-day variations of EEJ current (red legend) and magnetically five-quiet day average (black legend).

As part of our analysis, we incorporated 1-min-resolution geomagnetic data, specifically the SYM-H and ASYM-H indices (Figure 3e). The SYM-H and ASYM-H indices are indicators of the symmetric and asymmetric part of the ring current. The asymmetric or partial ring current occurs when hot ions from the tail region are injected into the evening and afternoon sectors, and subsequently drift and close in the ionosphere through field-aligned currents at dusk and dawn. By examining the enhancements in the ASYM-H index, we can gain insight into the occurrence of substorm injections and field-aligned current systems, which contribute to the asymmetry in the ring current [71,72].

To investigate the impact of geomagnetic storms and auroral substorms on the ionosphere over the Brazilian equatorial region, we analyzed the *Diono* current. By employing the *MRA-MODT* technique, we separated the  $DP2$  and  $D_{dyn}$  components from the *Diono*

current. The fluctuations in the  $DP2$  current are shown in Figure 3f. Figure 3g depicts the equatorial electrojet ( $EEJ$ ) in the Brazilian longitudinal sector. The red legend represents the day-to-day variation of the  $EEJ$  observed from 6 to 30 June 2015, while the black legend represents the average  $EEJ$  during five magnetically quiet days in June 2015. The  $DP2$  current is linked to the prompt penetration of the magnetospheric convection electric field at the magnetic equator during the main phase of geomagnetic storms [14–16,18,73]. In contrast,  $Ddyn$  represents the magnetic signature of ionospheric disturbance dynamo induced by Joule heating in the auroral zone (Blanc and Richmond 1980) [24]. In the low-latitude ionosphere,  $Ddyn$  exhibits a westward orientation during the day and an eastward orientation during the night. These phenomena have been investigated extensively by various researchers [17,24,54,58,60,65,74].

On 8 June, we observed a geomagnetic storm driven by a co-rotating interaction region (CIR) followed by high-speed solar wind streams (HSSWs). Figure 3a shows the increase in the solar wind speed from  $\sim 371$  km/s at 00:17, reaching a maximum speed of  $\sim 680$  km/s at approximately 11:52 UT on 8 June and remaining at an average of 500 km/s until 16 June 2015. Figure 3b shows that IMF Bz oscillated rapidly during the early hours of 8 June and turned southward at 06:25 UT, with a minimum southward incursion of  $\sim -20$  nT for 1 h. During the southward incursion of IMF Bz, the y component of the interplanetary electric field (IEyF) turned eastward (see Figure 3c), and it reached a maximum eastward amplitude of  $\sim 9$  mV/m at 06:25 UT. As shown in Figure 3d, the auroral westward electrojet (AL black legend) activities intensified on 8 June, starting from 06:00 UT, reaching a maximum westward value of  $-1068$  nT at 07:23 UT, and fluctuated continuously until 18 June 2015, under the influence of HSSWs (see Figure 3a). The southward incursion of the IMF Bz on 8 June triggered a moderate geomagnetic storm, as seen in the SYM-H and ASYM-H indices in Figure 3e. The main phase of the 8 June geomagnetic storm lasted 1.26 h. The recovery phase started at 07:40 UT on 8 June and lasted until 20 June 2015.

Another geomagnetic storm commenced from 18:38 UT on 22 June to 04:25 UT on 23 June 2015. Before the commencement of the 22 to 23 June geomagnetic storms, three interplanetary shocks (IS) hit the Earth's magnetic field [42,43,73].

The first IS arrived on 21 June at 17:00 UT, and the solar wind speed was increased from 300 to 400 km/s. This compressed the magnetopause and caused a sudden increase of approximately 40 nT in the SYM-H index, which lasted for 4.5 h (Figure 3d). However, the IMF Bz component remained positive, so no auroral electrojet activities followed, as seen in AU and AL (see Figure 3e) during this period. The second IS arrived on 22 June at approximately 04:45 UT and was accompanied by little enhancement in the solar wind speed from 400 km/s to  $\sim 500$  km/s, which provoked a short-duration of 20 to 27 nT increase in the SYM-H index (see Figure 3d). Unlike the two previous events, the arrival of the third IS was followed by giant coronal mass ejection (CME) at 18:38 UT on 22 June. The CME was accompanied by a significant increase in solar wind speed ( $V_{sw}$ ) from  $\sim 450$  to  $\sim 712$  km/s at 18:55 UT (Figure 3a). This CME caused significant oscillations in the IMF Bz component (see Figure 3b), provoking an increase of approximately 88 nT in the SYM-H index at 18:38 UT (see Figure 3d). At the IS3 arrival, the IMF Bz component was intense and directed southward (see Figure 3b), which led to magnetic reconnection and the development of a strong geomagnetic storm, with a minimum SYM-H index value of  $-208$  nT at 04:25 UT on 23 June 2015, and a maximum of 363 nT of the ASYM-H index at 19:50 UT on 22 June 2015.

One of the main features of this storm was the multiple large-amplitude fluctuations of IMF Bz during the main and recovery phases. The IMF Bz was first largely negative (southward) from 18:38 to 19:24 UT with the minimum of  $\sim -39$  nT at  $\sim 19:24$  UT on 22 June, which was the most negative excursion measured in 2015 [42,43] then turned positive (northward) for  $\sim 1.5$  h with the maximum of  $\sim 30$  nT at 20:36 UT. From  $\sim 20:55$  UT to 21:15 UT, IMF Bz was directed southward, and from  $\sim 21:25$  UT, IMF Bz turned northward and remained until 00:50 UT on 23 June. Between 00:55 and 01.8 UT, there were rapid small-amplitude fluctuations of IMF Bz, and from  $\sim 01:55$  UT, the Bz component decreased sharply to  $-28$  nT at 02:05 UT on 23 June and remained intensively negative until 05:30 UT. The

IMF Bz oscillations continued until ~12:00 UT during the recovery phase, which started at ~04:25 UT on 23 June, as seen from the SYM-H index behavior in Figure 3d. Following these IMF Bz oscillations, the interplanetary electric field (IEyF) component varied between −18 mV/m at 20:36 UT and +27 mV/m at 19:24 UT on 22 June and −21 mV/m at 00:36 UT and 20 mV/m at 02:06 on 23 June (see Figure 3c and Table 1).

**Table 1.** The minimum and maximum magnitudes of the parameters plotted in Figure 3 and their respective times of occurrence in universal time.

Day		Bz (nT)	Vsw (km/s)	IEyF (mV/m)	AL (nT)	AU (nT)	SYM-H (nT)	ASYM-H(nT)	EEJ (nT)	DP2 (nT) Belem	DP2 (nT) Alta Floresta
6	Min	−7.07	276.10	−2.01	−178	15	5	4	−41.65	−2.15	−1.18
	time	11:43	0:01	13:23	13:35	18:17	17:17	3.28	12:05	12:00	5.55
	Max	6.67	329.20	2.23	0	197	28	33	10.86	2.34	1.34
7	time	4:40	18:20	11:43	5:47	12:28	5:53	16:20	18:30	12:35	0:13
	Min	−9.92	292.40	−5.07	−270	12	−16	5	−7.96	−1.70	−1.48
	time	20:47	02:59	22:46	21:24	01:53	07:37	04:17	10:09	19:22	23:37
8	Max	14.21	402	3.62	−1	238	28	47	58.56	1.82	1.80
	time	16:56	23:31	20:47	18:14	05:23	13:3	20:55	15:26	19:44	00:00
	Min	−20.16	371	−6.36	−1068	23	−105	5	−29.55	−13.16	−5.21
9	time	06:25	00:17	10:17	07:23	07:17	07:46	03:34	10:25	11:20	11:19
	Max	12.25	680.40	9.38	−14	642	23	116	59.61	12.95	5.48
	time	09:34	11:52	06:25	04:27	06:31	00:08	07:07	16:21	11:46	11:43
10	Min	−5.32	578.40	−3.75	−710	13	−47	7	−11.99	−7.81	−5.05
	time	01:05	04:27	10:01	02:34	10:54	00:01	13:05	10:16	14:43	14:41
	Max	6.18	667.90	3.33	−22	368	−21	69	61.70	7.31	4.69
11	Time	10:01	13:18	01:05	11:02	22:56	13:14	02:47	16:52	16:52	15:01
	Min	−3.94	591.20	−2.61	−674	16	−38	7	−26.80	−5.01	−4.00
	time	00:10	00:45	01:53	00:54	14:38	00:53	13:26	10:58	10:57	01:22
12	max	4.17	667.90	2.46	−13	304	−18	55	31.53	4.57	4.72
	time	01:53	15:25	17:04	03:17	08:56	05:54	06:28	15:57	13:16	01:00
	Min	−3.82	495.70	−2.13	−722	8	−37	4	−42.00	−3.38	−3.47
13	time	02:41	00:00	09:11	04:04	09:53	03:55	15:24	11:27	13:50	03:42
	max	3.58	624.70	2.28	−9	282	−16	59	29.10	3.90	2.46
	time	09:11	03:30	02:39	20:40	03:34	07:07	03:59	14:42	12:04	04:04
14	min	−4.72	445.30	−3.25	−268	8	−24	5	−27.45	−6.13	−3.79
	time	15:47	15:42	20:42	05:31	09:30	00:14	23:17	10:35	15:50	15:49
	max	7.19	555.10	2.14	−12	179	30	51	32.27	6.5	3.61
15	time	20:42	23:04	15:47	20:51	05:32	17:57	18:44	17:59	16:10	16:10
	min	−5.95	449.40	−3.02	−444	24	−24	8	−15.91	−4.29	−2.59
	time	23:52	19:30	22:27	06:38	15:02	18:54	16:24	10:22	15:45	15:43
16	max	6.1	533.10	2.94	−6	276	2	49	45.36	4.19	2.50
	time	22:27	00:13	23:52	21:23	07:31	23:23	06:28	16:07	16:07	16:05
	min	−7.29	441.60	−5.86	−925	16	−35	5	−38.39	−5.38	−2.98
17	time	08:48	04:03	11:08	09:43	16:01	09:26	19:26	10:40	11:24	16:58
	max	10.61	635.30	3.54	−6	512	−6	82	41.87	7.03	3.91
	time	11:08	15:39	08:54	14:18	09:40	07:21	07:48	16:36	16:39	16:37
18	min	−4.94	484.40	−3.86	−968	14	−31	6	−48.39	−6.55	−3.96
	time	11:50	23:39	00:20	09:50	01:54	12:20	07:43	11:35	14:02	14:01
	max	6.69	628.80	2.89	−16	465	−5	60	16.98	6.52	3.77
19	time	00:23	00:13	11:50	01:11	14:10	18:13	18:32	14:32	14:26	14:24
	min	−5.93	460.60	−4.50	−588	18	−36	8	−19.58	−4.10	−2.53
	time	00:24	15:22	20:12	01:15	22:56	08:59	13:34	10:41	15:19	15:17
20	max	8.12	587.2	3.24	6	306	−8	64	38.72	4.89	2.10
	time	20:06	19:53	00:24	20:19	00:30	21:34	08:30	15:40	15:40	15:38

Table 1. Cont.

Day		Bz (nT)	Vsw (km/s)	IEyF (mV/m)	AL (nT)	AU (nT)	SYM-H (nT)	ASYM-H(nT)	EEJ (nT)	DP2 (nT) Belem	DP2 (nT) Alta Floresta
17	min	−6.79	410.20	−4.12	−677	14	−47	11	−27.07	−10.72	−4.16
	time	14:12	23:23	00:35	10:32	23:56	09:53	01:07	10:49	13:51	15:00
	max	7.71	554.60	3.12	0	428	−12	75	38.77	13.33	5.70
18	time	00:35	00:23	14:14	20:55	09:34	00:38	13:46	14:35	13:29	13:27
	min	−4.51	394.70	−2.14	−351	13	−32	3	−16.78	−2.80	−2.18
	time	12:20	18:37	06:29	02:26	00:14	00:11	12:02	11:15	15:20	15:18
19	max	4.99	465.20	1.97	−10	249	−16	36	53.45	3.03	2.33
	time	06:29	12:36	12:20	20:33	02:54	23:27	13:01	16:43	13:21	02:32
	min	−3.79	309.20	−1.43	−292	13	−25	2	−26.58	−1.83	−1.04
20	time	10:57	23:49	14:28	01:26	22:19	01:47	19:30	10:53	11:57	00:51
	max	4.26	412.30	1.36	−8	206	−12	37	39.83	1.71	1.15
	time	14:29	00:05	10:57	17:32	04:28	16:21	01:20	16:47	12:20	01:11
21	min	−2.26	279.70	−0.94	−53	9	−16	2	−24.21	−1.46	−1.22
	time	03:23	20:24	01:41	13:15	02:56	00:01	01:16	11:02	00:32	00:33
	max	2.76	342.70	0.68	−8	39	−1	18	33.39	3.29	2.80
22	time	01:41	01:30	03:23	07:49	13:47	21:04	12:57	16:44	00:10	00:10
	min	−5.73	277.10	−3.41	−151	8	−9	2	−37.57	−2.55	−3.74
	time	20:27	08:44	23:31	21:48	04:27	07:54	06:36	10:58	16:39	16:31
23	max	10.06	360.30	1.98	−1	113	46	70	20.64	3.35	4.69
	time	23:31	21:42	20:27	06:58	17:18	17:55	16:51	19:05	17:00	16:51
	min	−38.98	328.20	−18.35	−1508	4	−139	9	−65.23	−24.33	−22.58
24	time	19:24	00:29	20:36	18:57	19:57	20:18	12:44	18:35	18:29	20:01
	max	29.70	712.10	26.57	2	1473	88	363	88.96	21.32	24.52
	time	20:36	18:55	19:24	11:45	20:08	18:38	19:50	19:26	18:50	19:39
25	min	−28.05	516.80	−21.09	−1535	−23	−208	57	−147.78	−7.94	−6.67
	time	02:05	13:06	00:38	04:39	09:05	04:25	02:18	12:53	14:40	01:41
	max	32.21	781.80	20.01	19	1503	−57	172	19.20	9.25	8.14
26	time	00:38	03:56	02:06	01:48	01:46	19:32	04:45	00:14	14:20	01:17
	min	−6.70	530.10	−4.94	−792	14	−99	5	−54.63	−4.05	−4.15
	time	00:11	11:02	14:37	00:41	21:05	00:43	08:15	11:28	18:12	00:36
27	max	7.19	792.90	4.03	6	420	−37	77	46.40	4.60	5.22
	time	14:37	14:21	14:19	19:41	09:24	16:16	00:49	16:45	00:12	00:11
	min	−11.91	529.10	−8.68	−1005	17	−90	6	−72.66	−10.16	−4.94
28	time	08:50	22:29	07:57	07:48	04:37	19:44	08:35	14:54	13:33	13:28
	max	13.13	688.30	7.63	−20	586	−19	88	42.05	6.52	4.75
	time	07:57	09:34	08:50	05:52	13:49	05:39	07:44	17:56	13:52	09:13
29	min	−3.79	456.50	−1.77	−638	−6	−72	12	−37.36	−2.59	−2.66
	time	08:09	23:15	07:42	09:22	12:42	01:17	08:57	11:16	02:52	02:51
	max	3.34	580.30	2.14	−17	229	−36	67	5.40	2.19	2.32
30	time	07:38	10:18	08:09	17:50	02:45	23:23	00:12	23:57	03:12	02:31
	min	−6.08	390.50	−5.84	−329	−2	−48	5	−41.07	−3.74	−2.20
	time	23:45	21:51	04:34	23:25	21:19	01:10	22:52	10:46	13:23	13:21
31	max	9.02	825.10	3	−8	268	−22	45	13.76	4.00	2.33
	time	15:02	04:56	23:45	15:19	00:00	03:19	09:32	16:16	13:45	13:43
	min	−7.23	386.90	−1.82	−673	7	−63	6	−41.80	−6.83	−3.96
32	time	05:29	21:07	19:36	05:51	23:53	06:23	00:32	11:40	15:05	15:03
	max	4.62	519.90	3.34	−21	341	−28	68	19.31	8.45	5.01
	time	19:36	01:59	05:29	23:24	05:52	18:10	05:28	14:41	14:43	14:41
33	min	−5.59	336.40	−2.53	−397	−1	−41	5	−42.27	−3.32	−1.81
	time	07:29	22:39	09:09	08:48	03:42	00:01	11:37	11:02	11:54	07:52
	max	6.63	449.50	2.33	−6	150	−15	32	3.08	3.66	1.63
34	time	09:09	04:37	07:29	17:04	05:19	16:21	15:47	15:14	11:34	06:28
	min	−5.28	356	−1.94	−207	5	−29	2	−15.52	−3.26	−2.77
	time	05:39	22:00	02:04	17:51	03:10	00:01	10:26	10:12	23:50	23:48
35	max	4.96	414.50	2.13	−6	308	−2	35	33.45	1.94	2.17
	time	02:04	08:25	05:39	05:17	05:54	21:57	17:32	15:01	06:14	06:16

To examine the impacts of geomagnetic disturbances on the Brazilian equatorial ionospheric electric field during the June 2015 geomagnetic storms, Figure 3f,g present the *DP2* current fluctuations at magnetic stations in Belem (dip lat:  $-0.47^\circ$  in the red legend) and in Alta Floresta (dip lat:  $-3.75^\circ$  in the black legend) and the equatorial electrojet (*EEJ*: day-to-day variations of *EEJ* in the red legend and average of five magnetically quiet days presented in black legend in Figure 3g) in the Brazilian longitudinal sector, respectively.

On 8 June, we observed a remarkable increase in fluctuations of *DP2* current amplitude in Belem (red legend) during the daytime in the early stage of the recovery phase, but the amplitude of *DP2* at Alta Floresta (black legend) was less conspicuous. This observation provides evidence of the prompt penetration of the magnetospheric convection electric field (EPPEF) into the Brazilian equatorial ionosphere, as the Earth's ionosphere was influenced by HSSWs during the recovery phase on 8 June 2015. During the recovery phase of the 8 June storm, no significant decrease in the amplitude of the eastward *EEJ* was observed. The notable decrease in eastward *EEJ* amplitude during the daytime on 15 and 17 June 2015, showed the effect of westward disturbance dynamo on *EEJ* current.

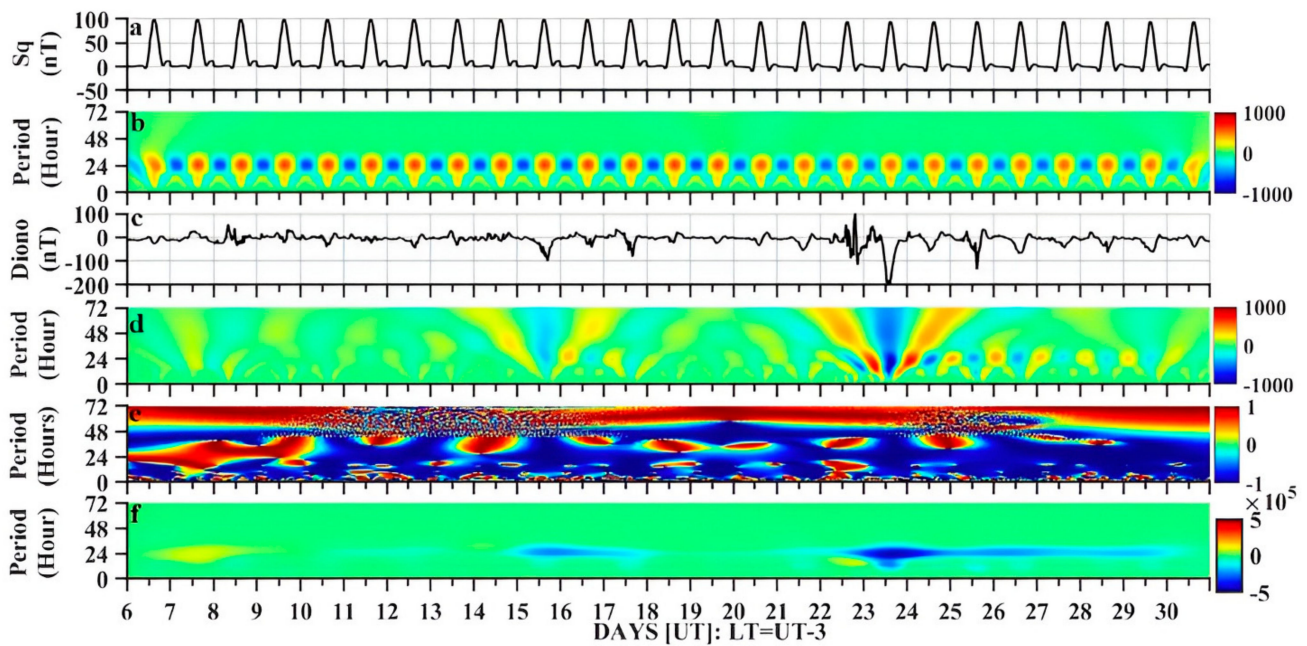
During the main phase of 22–23 June 2015, particularly on the dayside on 22 June, conspicuous fluctuations in the amplitude of *DP2* current between 18:25 and 20:00 UT in Belem (dip lat:  $-0.47^\circ$  presented in the red legend) and Alter Floresta (presented in the black legend) signaled the penetration of the PPMEF into the Brazilian equatorial ionosphere. The eastward maximum amplitude of the *EEJ* was 88.96 nT at 19:26 UT on 22 June, showed the effect of eastward PPMEF in the Brazilian magnetic equator. During the recovery phase on 23 June, *EEJ* westward flow was caused by westward disturbance dynamo electric field [22,24,59,74].

Table 1 shows the time intervals in Coordinated Universal Time (UTC) for the interplanetary parameters, including IMF Bz, Vsw, and IEyF, to change from minimum to maximum amplitudes during space weather events in June 2015. Additionally, it displays the time intervals for the AU, AL, SYM-H, ASYM-H, *EEJ*, and *DP2* currents to shift from minimum to maximum amplitudes in response to variations in the interplanetary parameters. Days with significant magnetic disturbances are highlighted in red, while all other days are shown in black. As shown in Table 1, there was no relationship between the time when the IEyF reached its maximum eastward amplitude on 8 June and the time when the *EEJ* reached its peak eastward amplitude. One possible explanation for this is that the main phase of the 8 June geomagnetic storm occurred at night in the Brazilian longitudinal sector. However, a correlation was found between the time at which Vsw reached maximum speed and the periods of *DP2* current fluctuations in Belem and Alta Floresta. On 22 June, the IMF B reached the minimum southward incursion of  $-38.98$  nT at 19:24 UT, while the IEyF reached maximum eastward amplitude of 26.57 mV/m at the same time. The impact of the IEyF's maximum eastward amplitude on the *EEJ* was evident, as it reached a maximum eastward value of 88.96 nT at 19:26 UT, just two minutes later. This serves as clear evidence of the eastward PPMEF in the Brazilian magnetic equatorial ionosphere during the dayside main phase on 22 June 2015, which was a geomagnetic storm. The PPMEF also caused fluctuations in the *DP2* currents in Belem and Alta Floresta on 22 June, as seen in columns 11 and 12, respectively. Moreover, the westward auroral electrojet reached a maximum negative amplitude of  $-1508$  nT at 18:57 UT, 19 min after the IMF Bz turned southward, whereas the eastward auroral amplitude reached a maximum positive amplitude of 1473 nT at 20:08 UT, 44 min after the IMF Bz reached its lowest southward incursion.

### 3.1.2. Phase Comparison between the Sq and Diono Currents in Belem from 6 to 30 June 2015

Figure 4 shows a phase comparison between the *Sq* (Figure 4a) and *Diono* currents (Figure 4c) from 6 to 30 June 2015. The wavelet-based method, called semblance analysis, compares the local phase relation between *Sq* and *Diono* currents as a function of time and wavelength (Figure 4b,d present the continuous wavelet transforms of *Sq* current and *Diono* current, respectively). The normalized amplitude of the local phase relationship between the *Sq* and *Diono* currents are presented in Figure 4e. The red legend in the color

bar represents the positive phase correlation (given as +1), and the anti-phase correlation is represented by the blue legend in the color bar (given as -1) [54,64,65]. The *anti-Sq* current is the signature of *Ddyn* [54,59,75–77]. Additionally, *Ddyn* can be influenced by other sources, such as the partial ring current during the early phase of a storm and *Sq-like* oscillations during the recovery phase, which are not associated with *Ddyn* [57]. Therefore, relying solely on filters to estimate the *Ddyn* from *Diono* may not yield accurate results. Figure 4f presents the amplitude of the semblance computed by applying Equation (10) in Cooper and Cowan (2008). The blue color in Figure 4f shows the days with development of *Ddyn*. We observed the development of *Ddyn* from 15 to 17 June as a result of the magnetic disturbance that occurred on 14 June, and it had a three-day duration. The intense amplitude of *Ddyn* developed from 23 to 29 June 2015, as a result of the intense geomagnetic storm of 22–23 June and had a duration of six days.



**Figure 4.** Phase comparison between *Sq* and *Diono* currents at Belem from 6 to 30 June 2015. (a) *Sq* current in Belem from 6 to 30 June 2015. (b) Continuous wavelet transforms (CWT) of the *Sq* current at Belem, and (c) *Diono* current at Belem from 6–30 June 2015. (d) Continuous wavelet transforms (CWT) of the *Diono* current at Belem. (e) Semblance between *Sq* and *Diono* current. The value -1 represents the *anti-Sq* current, and +1 represents the phase correction of the *Sq* and *Diono* currents. (f) Amplitude of semblance analysis between *Sq* and *Diono* currents.

### 3.1.3. Effect of Cowling Conductivity on the Strength of *Ddyn*

The equatorial electrojet is an eastward current that flows daily along the dip equator and produces a large variation in the magnetic field [51,78]. Close to the magnetic equator, the magnetic inclination angle ( $I$ ) is approximately zero ( $I \approx 0$ ). In the E-region, the winds sweep the ions and leave behind the electrons. Electrons are not affected because the collision frequency with the neutral particle is much smaller than the gyro-frequency. Owing to the Hall effect, we have:

$$J_H = \sigma_H E_x \tag{14}$$

$$J_p = \sigma_p E_z \tag{15}$$

This current cannot flow through the layer, and charges accumulate on its borders. The accumulated charges generate an upward electric field ( $E_z$ ). The vertical current cannot flow because the situation is considered to be in a steady state. Then, a current arises to cancel the Hall current, which is called the Pedersen current, as shown in Equation (15).

This implies that:

$$\sigma_H E_x = \sigma_p E_z \tag{16}$$

$$E_z = \sigma_H E_x / \sigma_p \tag{17}$$

The zonal current in Equation (18) is calculated by adding the current produced by ( $E_z \times B$ ), the Hall current, and the current  $E_x$  (Pedersen current).

$$J_x = \left( \frac{\sigma_H^2}{\sigma_p^2} + 1 \right) \sigma_p E_x = \sigma_c E_x \tag{18}$$

$$\sigma_c = \left( 1 + \frac{\sigma_H^2}{\sigma_p^2} \right) \tag{19}$$

Equation (19) represents the cowling conductivity, which is responsible for the intensification of the electrojet at the magnetic equator.

Figures 5 and 6 display the development of  $Ddyn$  in relation to the auroral electrojet activities and effect of cowling conductivity on the  $Ddyn$  amplitude variations in the equatorial latitude. In Figure 5, we present the diurnal component of  $Ddyn$  (see Figure 5c) at magnetic stations in Belem (dip lat:  $-0.47^\circ$  presented in red) and Alta Floresta (dip lat:  $-3.75^\circ$  presented in the black legend) alongside the Akasofu index (Figure 5a plotted on the left-hand side in the red legend), the AE index (plotted on the right-hand side and presented in the black legend), and the ASYM-H index in Figure 5b.

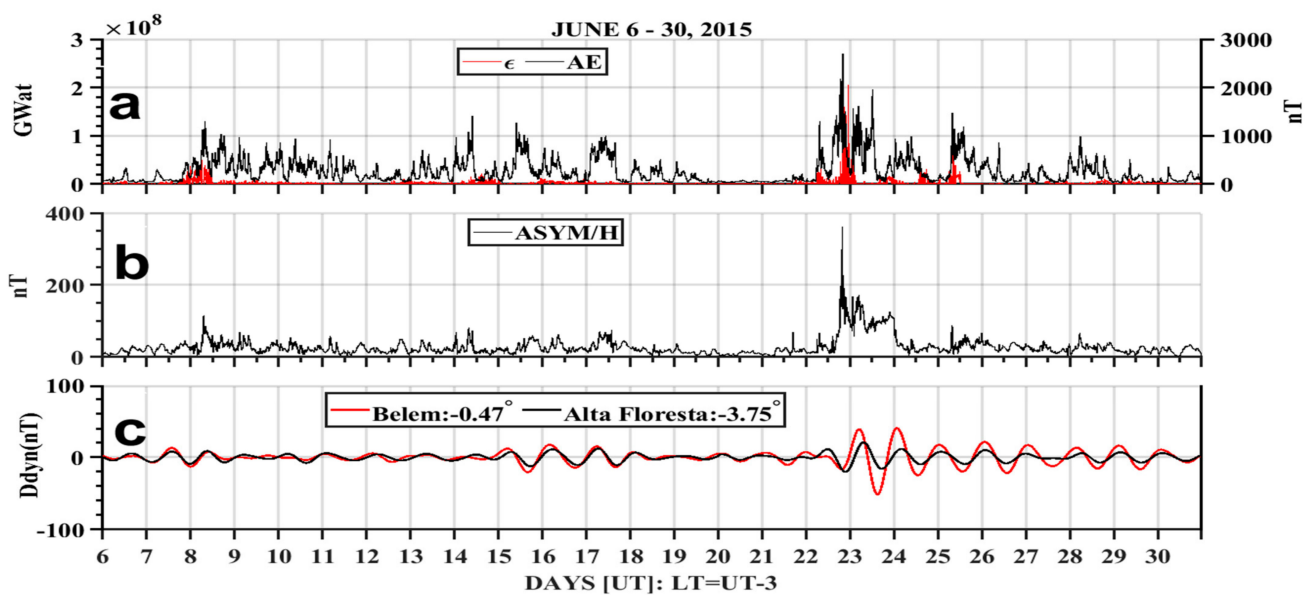


**Figure 5.** Variation in diurnal component of  $Ddyn$  alongside the AE index, Akasofu index, and ASYM-H index from 6 to 30 June 2015. (a) Day-to-day variation of the AE index (right-hand side of (a), presented in the black legend) and Akasofu index left-hand side of (a) presented in the red legend (b) ASYM-H index presented in (b). (c) Diurnal component of  $Ddyn$  at magnetic stations in Belem represented in the red legend and Alta Floresta represented in the black legend.

The Akasofu index shows the coupling between the magnetosphere and solar wind during geomagnetic storms and provides insights into the amount of energy poured into the magnetosphere by the solar wind–magnetosphere interaction and the response of auroral electrojet activities (AE index) to variations in the Akasofu index from June 6 to 30, 2015. During the main phase of the geomagnetic storm on June 8, 2015, the AE index responded promptly to the Akasofu index without a time delay. However, during the main phase of the geomagnetic storm on June 22–23, 2015, the AE index response

to the Akasofu index variations showed a time delay at 23:00 UT on June 22 owing to the intensification of the storm. This phenomenon suggests decoupling between the ring current and auroral processes during intense storms, with respect to their dependence on solar wind energization [39].

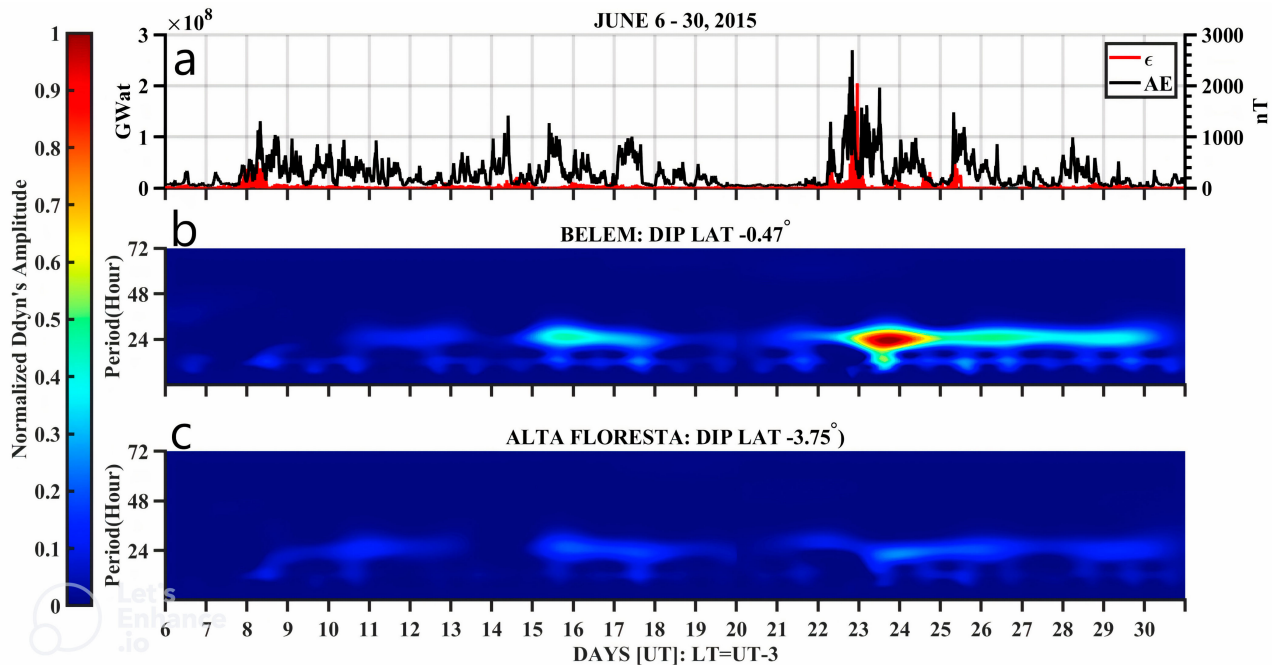


**Figure 6.** Development of *anti-Sq* amplitude computed from semblance cross-correlation wavelet analysis between *Sq* and *Diono* currents in relation to AE index activity and Akasofu index from 6 to 30 June 2015. (a) AE index plotted on the right-hand side (black legend) and Akasofu index plotted on the left-hand side (red legend) in (a). (b) *Anti-Sq* of semblance analysis of local phase comparison between *Sq* and *Diono* current at Belem (dip lat:  $-0.47^\circ$ ). (c) *Anti-Sq* of semblance analysis of local phase comparison between *Sq* and *Diono* currents at Alta Floresta (dip lat:  $-3.75^\circ$ ).

The Figure 5b presents the ASYM-H index. The ASYM-H index is a measure of the strength of the partial ring current. The ring current is asymmetric during the main phase of the 8 and 22–23 June 2015 geomagnetic storms. Obviously, the level of disturbance displayed by ASYM-H index during the main phase of the two storms corresponded with amount of energy derived from the solar wind–magnetosphere interaction which determined the amount of the energy input into the auroral ionosphere and magnetosphere as shown in Panel a by the Akasofu index and AE index. The ring current asymmetric magnitude was at the maximum during the main phase of 22–23 June and during the early stage of the recovery phase on 23 June (see Figure 5b), and the disturbance dynamo (*Ddyn*) presents in Figure 4c showed a remarkable eastward and westward amplitude on 23 June 2015, which corresponded with the period that intense magnetic perturbation was observed as seen on ASYM-H and AE indices. Our observations established that the strength of *Ddyn* at the low-latitude stations correlates with the magnitude of the auroral electrojet intensification in high-latitude auroral zone [35,54,74,79]. The *Ddyn* was observed six days after the main phase of 8 June (from 15–17 June 2015) geomagnetic storm and the maximum eastward amplitude on 15 June was 12 nT at 04:56 UT and maximum westward amplitude was  $-20$  nT at 16:03 UT in Belem and maximum eastward amplitude was 7.45 nT at 06:58 UT and maximum westward amplitude was  $-12.30$  nT in Alta Floresta. But, we started to observe the *Ddyn* development since the late stage of the main phase at 19:25 UT on 22 June, and the maximum westward amplitude was  $-16.33$  nT in Belem and  $-20.13$  nT at 21:31 UT in Alta Floresta, which established the interplay between the eastward PPMEF and westward DDEF during the main phase on 22 June as first mentioned by Singh et al.

(2017) and Astafyeva (2017, 2018). And, on 23 June, the maximum eastward amplitude in Belem was 39 nT at 05:01 UT and maximum westward amplitude was  $-51.20$  nT at 15:00 UT and in Alta Floresta, the maximum eastward amplitude was 20.75 nT at 07:19 UT and the maximum westward amplitude was  $-15.75$  nT at 17:22 UT.

Figure 6 presents a normalized amplitude of  $D_{dyn}$  at two locations: Belem (refer to Figure 6b) and Alta Floresta (refer to Figure 6c). These amplitude values are juxtaposed with the Akasofu parameter (located on the left-hand side of Figure 6a and indicated by a red legend) and the AE index (found on the right-hand side of Figure 6a, denoted by a black legend).

Figure 6b,c represent the anti-Sq current amplitudes presented in Figure 4f. The X-axis is labeled in days, while the Y-axes of Panels b and c display the periods of oscillations of the  $D_{dyn}$  amplitudes in hours. The color index is shown in the leftmost column, representing the normalized amplitude of  $D_{dyn}$ .

A clear observation from Panels b and c is that the dominant periods of  $D_{dyn}$ , marked by a high-power spectrum, typically span approximately 24 h (diurnal). Notably, the highest amplitude was recorded during the strong storm recovery phase on 23 June 2015, which coincided with remarkable fluctuations in the AE and ASYM-H indices. The variations in the magnitude of the amplitude in Belem and Alta Floresta can be attributed to the effect of cowling conductivity, which is strongest in Belem and tends to enhance the amplitude of  $D_{dyn}$  there.

Table 2 displays the minimum and maximum indices of Akasofu, AE, ASYM-H, and  $D_{dyn}$ , as well as the time at which each index reached its individual minimum and maximum values, in response to the space weather event that occurred in June 2015. Days with magnetic disturbances are highlighted in red. The data in Table 2 reveal that the time lag between the maximum Akasofu index and the maximum eastward amplitude of the AE index was 1.40 h on 8 June and 2.02 h on 9 June. This delay may have hindered the development of  $D_{dyn}$  during the recovery phase of the geomagnetic storm on 8 June. On 14 June, we observed that the AE index reached its maximum eastward value of 1418 nT at 09:42 UT, whereas the Akasofu index reached its maximum value of  $2.20 \times 10^7$  GW at 14:49 UT. This indicates that the AE index reached its maximum amplitude 5.07 h before the Akasofu index, suggesting a long duration of coupling between the solar wind and the magnetosphere. This could have contributed to the development of  $D_{dyn}$  at the Brazilian magnetic equatorial latitude from 15 to 17 June 2015.

During the geomagnetic storm of 22–23 June 2015, we observed a rapid response between the Akasofu and AE indices. Table 2 illustrates that on 22 June, the Akasofu index reached peak value of  $2.32 \times 10^8$  GW at 20:13 UT, while the AE index attained maximum eastward amplitude of 2698 nT at 20:10 UT. This signifies that the AE index reached maximum eastward amplitude three minutes after the Akasofu index reached peak value. The significant energy transfer from the solar wind to the magnetosphere due to solar wind–magnetosphere coupling resulted in Joule heating in the auroral high-latitude ionosphere, which drove the disturbed equatorward wind and led to the development of the westward  $D_{dyn}$ . We observed the maximum westward amplitude of  $-16.33$  nT at 19:25 UT in Belem and  $-20.13$  nT at 21:31 UT in Alta Floresta on 22 June 2015. The maximum westward amplitude of  $D_{dyn}$  was registered on 23 June at 15:00 UT in Belem, with a value of  $-51.20$  nT and at 17:22 UT in Alta Floresta with a value of  $-15.75$  nT. Table 2 reveals that the time lag between the Akasofu maximum index and the AE maximum index was smaller during the 22–23 June geomagnetic storm than during the 8 June geomagnetic storm. Additionally, the data in Table 2 show that the disturbance wind first reached Belem, which is closer to the magnetic equator before Alta Floresta. Zhang et al. (2017) found that disturbance winds tend to approach the magnetic equator more easily in the Northern Hemisphere's Asian sector, because the magnetic equator is located in the Northern Hemisphere and is associated with greater heating rates in the summer hemisphere and prevailing summer-to-winter winds [79].

**Table 2.** Minimum and maximum Akasofu index, AE index, ASYM-index, *Ddyn* at Belem, and Alta Floresta along with the time of occurrence.

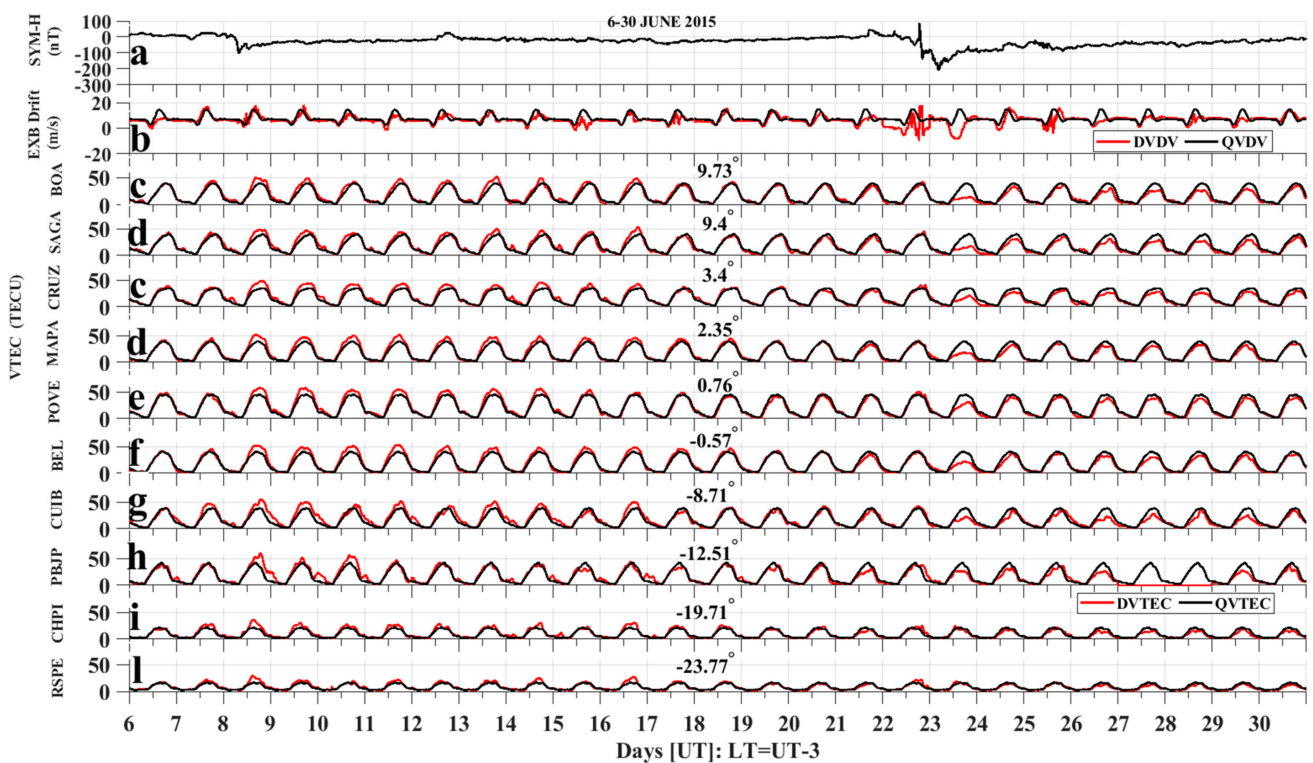
DAY		Akasofu Index (GW)	AE Index (nT)	ASYM-H Index (nT)	<i>Ddyn</i> (nT) at Belem (dip lat: $-0.47^\circ$ )	<i>Ddyn</i> (nT) at Alta Floresta (dip lat: $3.75^\circ$ )
6	Min	$1.4 \times 10^{-5}$	23	4	-4.58	-4.62
	Time	22:09	18:09	03:17	00:00	00:00
	Max	$7.06 \times 10^6$	336	33	2.51	5.38
7	Time	12:02	12:43	16:12	00:01	15:41
	Min	0	32	5	-12.84	-9.07
	Time	04:45	17:16	04:17	23:57	23:57
8	Max	$3.77 \times 10^7$	458	47	13.06	8.07
	Time	23:53	21:24	20:55	13:43	13:53
	Min	$2.09 \times 10^{-5}$	128	5	-12.84	-9.02
9	Time	17:24	03:26	03:34	00:01	00:01
	Max	$5.10 \times 10^7$	1310	116	7.57	8.71
	time	06:12	07:52	07:07	09:47	08:57
10	Min	0	41	7	-1.25	-2.22
	Time	08:21	10:56	13:05	09:09	18:42
	Max	$1.04 \times 10^7$	969	69	2.55	3.48
11	Time	12:32	02:34	02:47	18:20	05:06
	Min	$5.55 \times 10^{-5}$	41	7	-3.70	-7.69
	Time	13:47	04:50	13:26	14:46	15:05
12	Max	$5.63 \times 10^6$	945	55	4.52	5.02
	Time	04:08	09:06	06:28	00:00	00:00
	Min	0	40	4	-3.90	-4.30
13	Time	12:14	10:22	15:24	14:19	17:40
	Max	$3.28 \times 10^6$	933	59	4.78	5.88
	Time	04:51	04:04	03:59	01:10	02:04
14	Min	0	36	5	-6.32	-4.17
	Time	10:33	20:51	23:17	14:03	19:00
	Max	$1.12 \times 10^7$	437	51	5.52	4.28
15	Time	20:22	05:32	18:44	03:22	06:14
	Min	$3.89 \times 10^{-5}$	54	8	-3.57	-4.58
	Time	13:49	21:22	16:24	19:52	22:23
16	Max	$5.88 \times 10^6$	701	49	3.30	4.97
	Time	10:44	06:38	06:28	09:08	08:45
	Min	$1.90 \times 10^{-5}$	46	5	-2.56	-4.33
17	Time	20:11	15:38	19:26	15:18	00:01
	Max	$2.20 \times 10^7$	1418	82	5.36	3.87
	Time	14:49	09:42	07:48	00:00	00:00
18	Min	0	39	6	-20.52	-12.30
	Time	07:54	01:59	07:43	16:03	17:27
	Max	$1.20 \times 10^7$	1271	60	12.03	7.45
19	Time	23:10	09:51	18:32	04:56	06:58
	Min	0.0041	32	8	-14.39	-10.55
	Time	15:16	20:19	13:34	17:45	19:13
20	Max	$1.33 \times 10^7$	758	64	17.31	11.04
	Time	23:05	01:11	08:30	03:58	05:31
	Min	$6.35 \times 10^{-4}$	31	11	-13.43	-10.88
21	Time	23:30	22:20	01:07	16:02	16:41
	Max	$8.46 \times 10^6$	1007	75	15.22	12.12
	Time	00:58	10:32	13:46	05:42	06:33
22	Min	0	37	3	-3.24	-3.04
	Time	15:29	21:05	12:02	11:09	14:05
	Max	$4.02 \times 10^6$	523	36	7.52	6.56
23	Time	10:30	02:27	13:01	01:45	02:52
	Min	0.0047	30	2	-3.55	-2.95
	Time	04:48	16:26	19:30	13:51	17:12
24	Max	$3.30 \times 10^6$	472	37	5.057	1.92
	Time	13:03	01:26	01:20	00:00	00:00

Table 2. Cont.

DAY		Akasofu Index (GW)	AE Index (nT)	ASYM-H Index (nT)	Ddyn (nT) at Belem (dip lat: $-0.47^\circ$ )	Ddyn (nT) at Alta Floresta (dip lat: $3.75^\circ$ )
20	Min	3.11	28	2	−5.52	−3.42
	Time	08:27	04:16	01:16	12:12	11:53
	Max	$2.90 \times 10^6$	88	18	5.85	4.11
21	Time	02:04	13:15	12:57	00:00	02:11
	Min	0	29	2	−10.45	−3.67
	Time	15:10	06:44	06:36	13:52	13:43
22	Max	$9.21 \times 10^6$	223	70	7.38	2.43
	Time	18:27	21:48	16:51	23:39	00:01
	Min	$3.41 \times 10^{-4}$	48	9	−16.33	−20.13
23	Time	19:38	02:31	12:44	19:25	21:31
	Max	$2.32 \times 10^8$	2698	363	7.33	11.38
	Time	20:13	20:10	19:50	00:01	11:47
24	Min	0.0058	39	57	−51.20	−15.75
	Time	05:41	19:22	02:18	15:00	17:22
	Max	$9.73 \times 10^7$	1966	172	39.09	20.75
25	Time	01:30	12:14	04:45	05:01	07:19
	Min	$2.91 \times 10^{-4}$	20	5	−24.85	−9.62
	Time	08:23	21:05	08:15	12:59	14:27
26	Max	$3.33 \times 10^7$	984	77	40.40	11.61
	Time	14:46	09:32	00:49	01:38	04:01
	Min	$1.71 \times 10^{-5}$	50	6	−19.64	−9.34
27	Time	02:49	04:36	08:35	13:24	14:46
	Max	$7.21 \times 10^7$	1483	88	19.88	8.70
	Time	08:26	07:50	07:44	00:00	00:00
28	Min	$1.65 \times 10^{-4}$	26	12	−21.84	−8.39
	Time	06:52	13:00	08:57	13:42	13:15
	Max	$2.29 \times 10^6$	860	67	21.34	10.18
29	Time	09:47	09:21	00:12	01:29	01:58
	Min	$3.05 \times 10^{-4}$	18	5	−12.34	−2.17
	Time	14:11	06:28	22:52	14:33	20:43
30	Max	$7.99 \times 10^6$	585	45	17.07	5.21
	Time	21:32	23:56	09:32	01:07	00:01
	Min	$4.67 \times 10^{-5}$	36	6	−15.54	−7.34
31	Time	00:37	23:48	00:32	15:08	16:30
	Max	$1.07 \times 10^7$	994	68	13.42	5.81
	Time	18:54	05:52	05:28	03:45	06:30
32	Min	8.23	21	5	−16.39	−7.32
	Time	11:40	04:14	11:37	14:28	15:06
	Max	$1.06 \times 10^7$	523	32	16.08	7.14
33	Time	08:28	08:48	15:47	02:50	03:41
	Min	0	23	2	−6.82	−5.03
	Time	16:35	04:26	10:26	16:06	15:30
34	Max	$4.35 \times 10^6$	356	35	10.71	5.93
	Time	01:41	05:55	17:32	01:51	02:40

### 3.1.4. Response of Brazilian Equatorial and Low-Latitude Ionospheric Vertical Total Electron Content to Geomagnetic Disturbances of June 2015

Figure 7 presents the effects of geomagnetic disturbances on vertical  $E \times B$  drift velocity and ionospheric VTEC in the Brazilian longitudinal sector. Panel a shows the day-to-day variability of the SYM-H index from 6 to 30 June 2015. Panel b illustrates the day-to-day variability of vertical  $E \times B$  drift velocity (DVDV red legend), plotted along with average of five magnetically quiet days in the month of June 2015. Panels c–l, present day-to-day variability of VTEC from 6 to 30 June 2015 (DVTEC red legend) and the average of five magnetically quiet days in June 2015 (QVTEC black legend). The X-axes represent the days in universal time (UT).



**Figure 7.** Temporal variation of VTEC alongside the SYM-H index and  $E \times B$  drift velocity from 6 to 30 June 2015. (a) Day-to-day variability of SYM-H index from 6 to 30 June 2015. (b) Day-to-day variability of vertical drift velocity (DVDV: red legend) and average of five magnetically quiet days in June 2015 (QVDV; black legend). (c–l) Day-to-day variations of VTEC from 6 to 30 June 2015 (red legend) and average of five magnetically quiet days in June 2015 (black legend).

The geomagnetic storm of the 8 June main phase was on the nightside in the Brazilian longitudinal sector (03:20 LT to 04:46 LT; Table 1); therefore, no remarkable geomagnetic activities were observed during the main phase. The Earth's ionosphere was under HSSWs during the recovery phase from 07:45 UT on 8 June to 00:23 on 17 June 2015. During the recovery phase, from 12:00 UT on 8 June, we observed positive ionospheric storms from the Northern Hemisphere to the Southern Hemisphere (Figure 7c–l) as the value of the DVTEC (red legend) from 8 to 16 June 2015 was greater than the average of five magnetically quiet days (QVTEC black legend). The positive ionospheric storm was strengthened in the Southern Hemisphere EIA crest (from  $-12.51^\circ$  to  $-23.77^\circ$  dip latitude) on 8 June 2015 owing to enhancement in upward drift velocity of the ionospheric plasma, as seen in Figure 7b.

Moving to the 22–23 June 2015, the main phase of the geomagnetic storm spanned from 18:38 UT on 22 June to 04:25 UT on 23 June 2015. On the dayside of the main phase, on 22 June, we observed enhancement in the positive ionospheric storm for a short period in the Southern Hemisphere (from  $-12.51^\circ$  to  $-23.77^\circ$  dip latitude). The upward vertical drift of the plasma on the dayside of the main phase can be attributed to the effect of the eastward PPMEEF. The interplay of the eastward prompt penetration of the magnetospheric convection electric field and the westward disturbance dynamo electric field might be the cause of the short duration of the positive ionospheric storm during the main phase on 22 June 2015 in the Brazilian longitudinal sector.

During the recovery phase, on 23 June 2015, the westward disturbance dynamo electric field caused downward drift of the vertical  $E \times B$  drift velocity. The downward drift of the  $E \times B$  drift velocity lowered the ionosphere to a region of high recombination rate, and this effect was observed on 23 June 2015, as the average of five magnetically quiet days of VTEC in June 2015 was greater than the DVTEC on 23 June 2015.

Figure 8 encompasses three panels, elucidating the following: (a) On the left-hand side, it illustrates the storm-time residual of the equatorial electrojet ( $\Delta EEJ$ ) from 8 to 30 June 2015, represented in the black legend. The right-hand side of Panel a portrays the *Diono*, presented in the red legend. (b) Depicts the day-to-day variability of vertical total electron content (VTEC) in the Brazilian longitudinal sector. Additionally, the SYM-H index is illustrated on the right-hand side and indicated by the red curve. (c) The storm-time residual of VTEC ( $\Delta VTEC$ ) from 6 to 30 June 2015, featured on the TEC-MAP (the color bars are represented in the left-hand side of Panels c and b), and the Y-axes are the magnetic dip latitude, while the SYM-H index is plotted on the right-hand side and depicted as a red curve. Figure 8a reveals the influence of the *Diono* current on  $\Delta EEJ$ . On the dayside, the southward *Diono* current prompted  $\Delta EEJ$  to flow westward, particularly on 15, 17, 21, 23, and 29 June 2015. Conversely, the northward *Diono* current directed the  $\Delta EEJ$  eastward on 8 and 22 June 2015. In Figure 8c, the  $\Delta VTEC$  map reveals VTEC enhancement from 8 to 17 June, except for 15 June, when VTEC depletion was observed within the range of  $-10^\circ$  to  $-20^\circ$ , occurring at approximately 13:00 UT and 20:00 UT. VTEC enhancement was noticeable in both the Northern and Southern Hemispheres, ranging from  $10^\circ$  in the Northern Hemisphere to  $-18^\circ$  in the Southern Hemisphere. However, on 8 and 18 June, substantial enhancement at the EIA crest, ranging from 10 TECU to 20 TECU, was observed. This enhancement occurred between 12:00 UT and 23:00 UT on the respective days.

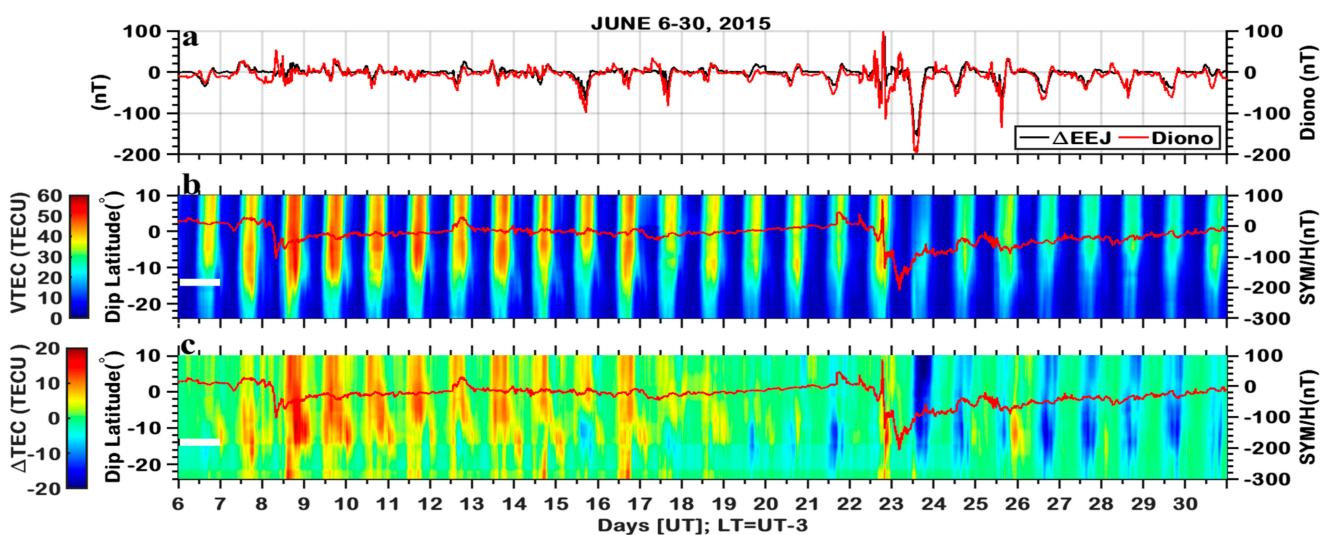


**Figure 8.** Spatial-temporal variation of VTEC from 8 to 30 June 2015. (a) Change in EEJ ( $\Delta EEJ$ ) from 6 to 30 June 2015, plotted on left-hand-side of (a) (black legend) and *Diono* current from 6–30 June 2015, plotted on right-hand side of Panel a of Figure 8 (red legend). (b) Day-to-day variability of VTEC from 6 to 30 June 2015 shown on TEC-MAP and day-to-day variability of SYM-H index plotted on right-hand side of (b) (red legend). (c) Change in VTEC ( $\Delta VTEC$ ) from 6 to 30 June 2015, shown on TEC-MAP and day-to-day variability of SYM-H index plotted on right-hand side (red legend) from 6 to 30 June 2015.

On 22 June, we observed positive ionospheric storms that ranged between 10 TECU and 20 TECU in the Southern Hemisphere from  $-4^\circ$  to  $-24^\circ$  dip latitude between 18:38 UT and 19:26 UT due to the effect of the eastward PPMF. On 23 June, we observed another less intense positive ionospheric storm that ranged from 2 to 8 TECU from 0:00 UT to 11:00 UT in the Northern Hemisphere and Southern Hemisphere ( $10^\circ$  to  $-10^\circ$  dip latitudes), which can be attributed to the eastward disturbance dynamo electric field.

During the recovery phase on 23 June, the VTEC exhibited varying degrees of depletion, notably from 23 to 29 June. On 25 June, a period of VTEC enhancement was detected within the range of  $-4^\circ$  to  $-20^\circ$ , coinciding with the intensification of the ring current, as indicated by the SYM-H index. This caused  $\Delta EEJ$  to shift eastward during the pre-reversal enhancement period. The VTEC depletion from 23 June to 29 June spanned from  $-20$  TECU to  $-5$  TECU

and occurred between 12:00 UT and 23:00 UT. Negative ionospheric storms were correlated with the influence of the westward disturbance dynamo, as shown in Figure 5c.

### 3.2. SAMI2 Model Run Results

Figures 9 and 10 present a comparative analysis of the daily average values between the SAMI2 model vertical total electron content (*SAMI2 model-VTEC*) and global positioning system (*GPS-VTEC*) within the Brazilian region from 6 to 30 June 2015. The Y-axis denotes the VTEC (in TECU), and the x-axis represents the magnetic latitudes in degrees. The *SAMI2 model-VTEC* is denoted in the red legend and the *GPS-VTEC* is identified in the black legend. The root mean square errors (RMSE) are indicated within each figure for each day. We input the daily average of the Ap index into the SAMI2 model to describe the geomagnetic activity levels, daily average of F10.7 cm and the three-month average of F10.7 cm was also input into the SAMI2 model. The HWM14 model provides neutral wind velocity, and the nrlmsise00 model provides neutral densities and temperature. The Fejer-Scherliess empirical model [26] was used as an input to the SAMI2 model to describe the ionospheric electric field during the magnetically quiet and auroral substorm periods.

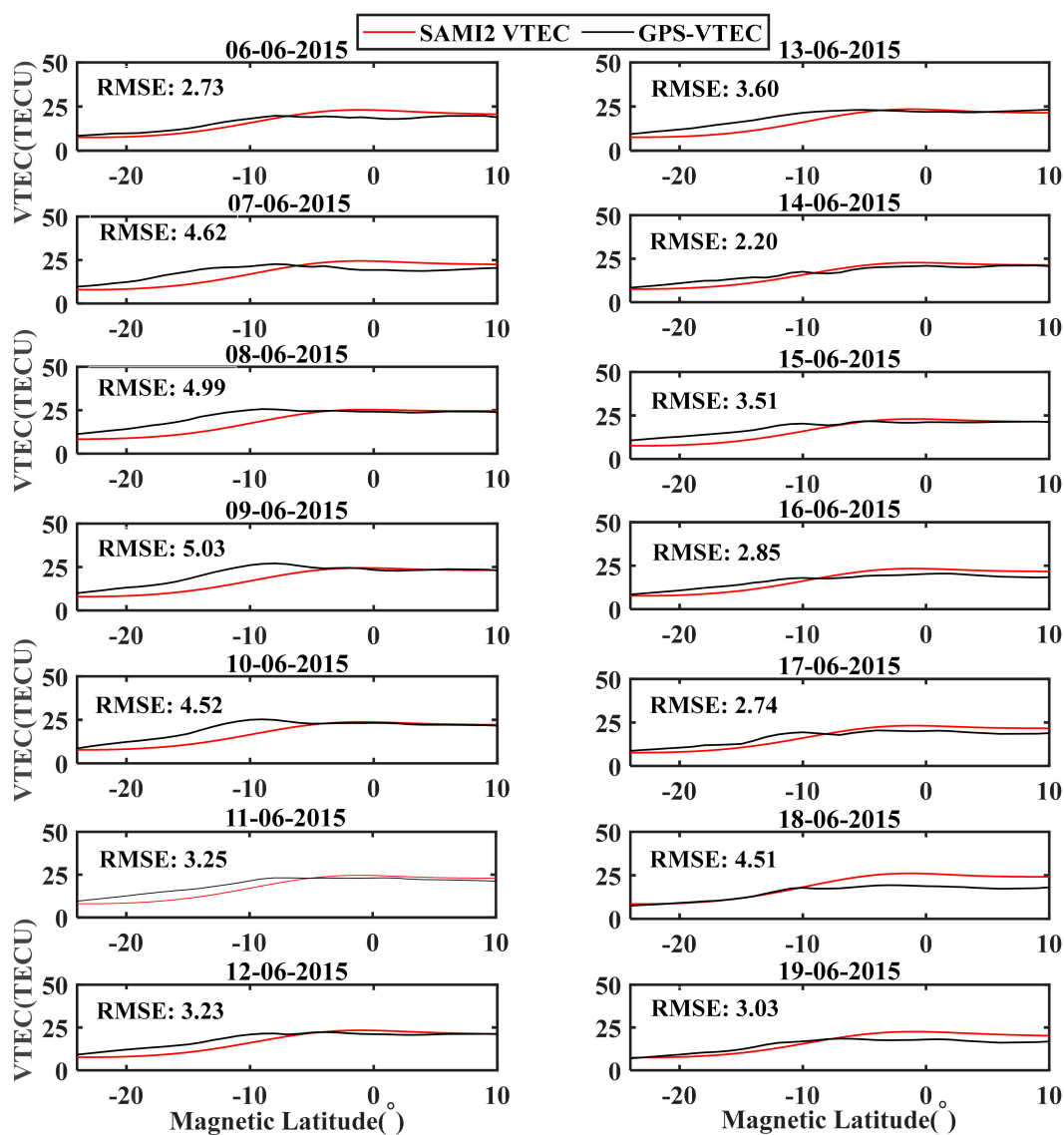


Figure 9. SAMI2 model-VTEC comparison with GPS-VTEC from 6 to 19 June 2015.

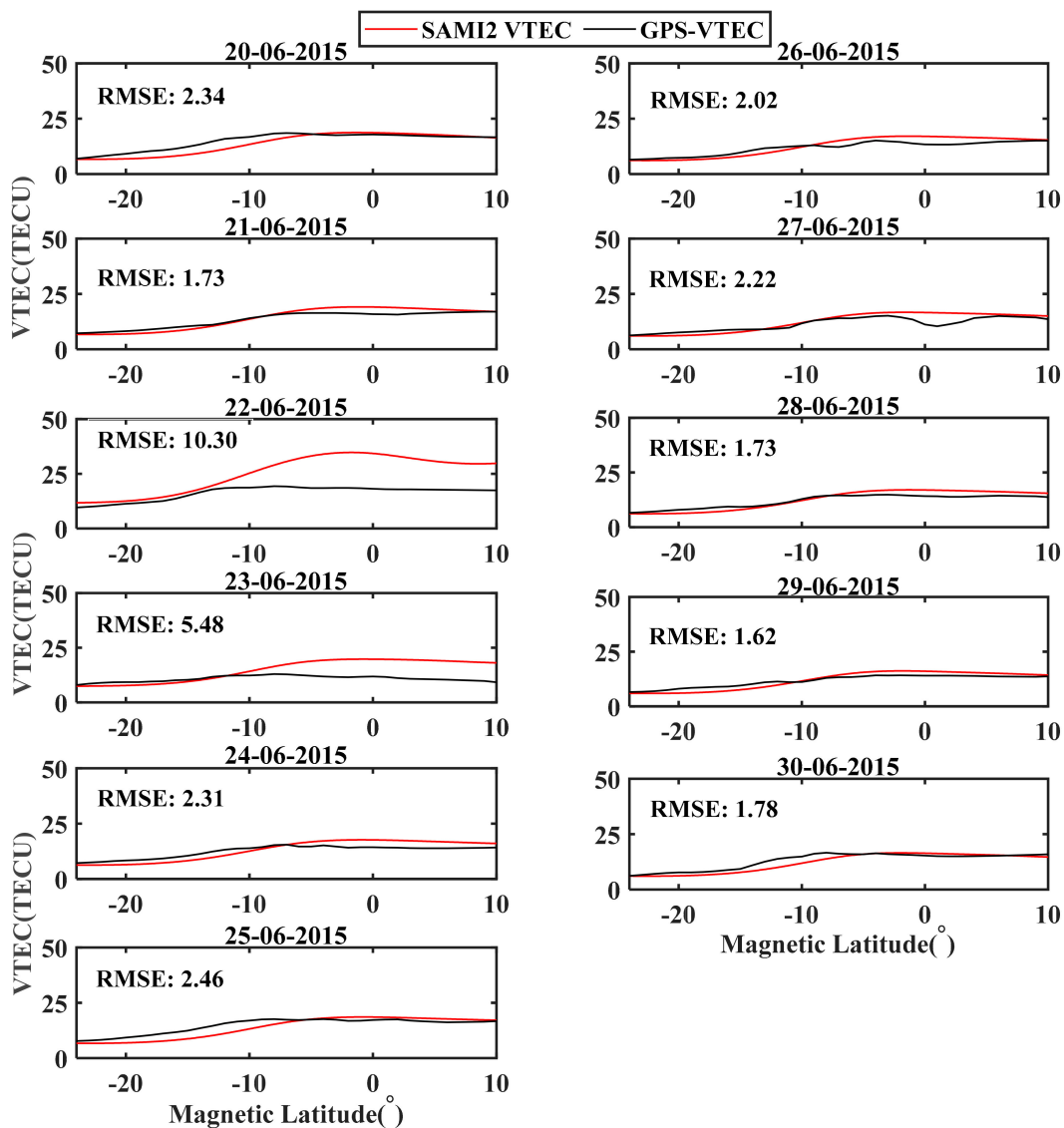


Figure 10. SAMI2 model comparison with GPS-VTEC from 20 to 30 June 2015.

Comparing the SAMI2 model-VTEC and GPS-VTEC in the two days preceding 8 June 2015, reveals RMSE values of 2.73 TECU and 4.62 TECU (see 6 and 7 June in Figure 9). Currently, the SAMI2 model overestimates the VTEC between  $-7^{\circ}$  and  $10^{\circ}$  magnetic latitude and underestimates it between  $-8^{\circ}$  and  $-24^{\circ}$  magnetic latitude. But, from 8–9 June, the RMSE values were 4.99 and 5.03 TECU, respectively, and the increase in RMSE on 8 and 9 June can be attributed to the effect of geomagnetic storm of 8 June. Subsequently, from 8 to 15 June 2015, the SAMI2 model-VTEC and GPS-VTEC demonstrated favorable agreement between the  $-7^{\circ}$  and  $10^{\circ}$  magnetic latitudes, but the SAMI2 model underestimated the VTEC between the  $-8^{\circ}$  and  $-24^{\circ}$  magnetic latitudes (in the Southern Hemisphere).

On 16 and 17 June, a recurrence of the pattern observed on 6 and 7 June occurred. June 18 showed a commendable agreement between the SAMI2 model-VTEC and GPS-VTEC from  $-24^{\circ}$  to  $\sim -10^{\circ}$  magnetic latitude, but the SAMI2 model overestimated VTEC from  $-10^{\circ}$  to  $+10^{\circ}$  magnetic latitude; the RMSE recorded on this day was 4.51 TECU.

Proceeding to the geomagnetic storm of 22–23 June 2015, the SAMI2 model-VTEC demonstrated concordance with the GPS-VTEC between  $-8^{\circ}$  and  $10^{\circ}$  magnetic latitudes during the magnetically quiet day on 20 June 2015. However, on 22 and 23 June, we recorded the biggest RMSE of 10.30 and 5.48 TECU (see Figure 10) respectively. The SAMI2 model overestimated the VTEC from  $-10^{\circ}$  to  $+10^{\circ}$  magnetic latitude in the Brazilian sector.

The minimum RMSE was documented on 29 June 2015 (1.62 *TECU*), as the Brazilian longitudinal sector ionosphere recovered from geomagnetic disturbances. The heightened RMSE on 22 June 2015 is attributed to the impact of geomagnetic disturbances arising from the competition between the eastward prompt penetration of magnetospheric convection electric field (EPPMEF) and the westward disturbance dynamo electric field. Similarly, the elevated RMSE on 23 June is linked to the westward disturbance dynamo electric field that induced westward flow of the equatorial electrojet (EEJ) during the daytime.

#### 4. Discussion and Conclusions

##### 4.1. Effects of IMF Bz Oscillations on DP2 Current Fluctuations in Brazilian Equatorial Latitude

The interaction between the solar wind and the Earth's magnetosphere induces the formation of region 1 (R1) and region 2 (R2) field-aligned current (FAC) systems, along with the associated magnetospheric plasma convection. Generally, the R1 and R2 FACs create an electric field that can generate a high-latitude current system exhibiting quasiperiodic fluctuations, which are closely correlated with variations in the interplanetary magnetic field (IMF) Bz component. The magnetic disturbance observed at the high-latitude ground level is primarily attributed to Hall currents, as the magnetic effects of Pederson currents cancel those of the FAC, but with opposite signs [29,80]. Consequently, DP2 fluctuations at high latitudes result from the combined influence of Hall conductivity and the solar wind-driven convection electric field [81–83]. These DP2 fluctuations rapidly extend to the equatorial ionosphere (refer to Figure 3f) through the transmission of TM0 mode waves in the Earth-ionosphere waveguide [80].

Figures 11 and 12 display the zoomed plots of the DP2 fluctuations alongside the IMF Bz and its effect on EEJ fluctuations on 8 and 22 June 2015 on the dayside (shown by the black rectangular box). The DP2 currents at Belem and Alta Floresta show a remarkable fluctuation during the daytime in response to northward and southward IMF Bz fluctuations. The effect of DP2 fluctuations in the equatorial zone also caused EEJ current to fluctuate, as presented in Panel a of Figures 11 and 12, respectively. On the night side of the main phase, DP2 currents did not show any remarkable fluctuations. This phenomenon established the observation of Nishida et al. (1968) that the interaction between the geomagnetic field and IMF Bz produced two reconnection locations, at the dayside (sunward side) and nightside (tailside), and that the field-aligned currents that originate from nightside reconnection may not be the cause of the DP2 current system, because the transit time of the event from the tailside reconnection region (away from the ground by tens to a few hundred RE) to the ground is much greater than the DP2 fluctuation time. This implies that field-aligned currents that originate from dayside reconnection drive the DP2 current system [16,80].

The equatorial electrojet also showed a remarkable response to the penetration of the y-component of the interplanetary electric field on 22 June to the Brazilian equatorial station. The EEJ reached the eastward maximum amplitude of  $\sim 88$  nT (19:26 UT) within 2 min after the IEyF reached maximum eastward amplitude of  $\sim 27$  mV/m at 19:24 UT on 22 June 2015. This is clear evidence of eastward prompt penetration of magnetospheric convection electric field into the equatorial ionosphere and enhancing the eastward EEJ component (see Figure 3f) [31,44].

##### 4.2. Development of Disturbance Dynamo Electric Field during Recovery Phase of June 2015 Geomagnetic Storm and Associated Positive and Negative Ionospheric Storms

The disturbance dynamo induced by storm-time disturbance winds becomes prominent during the recovery phase and persists for extended durations [84,85]. Blanc and Richmond (1980) [24] systematically elucidated the disturbance dynamo concept by simulating the impact of mid-latitude disturbance winds on the ionospheric electrodynamics. Their findings revealed equatorward winds propelled by high-latitude Joule heating deflecting westward at middle latitudes due to the Coriolis force. These deflected winds drive an equatorward current, creating a poleward electric field that counterbalances wind-induced

current. This electric field induces an eastward Hall current, resulting in positive (negative) charges accumulating at the dusk (dawn) terminator and establishing a dusk-dawn electric field. Richmond et al. (2003) [86] extended these simulations by combining winds driven by high-latitude plasma convection and Joule heating, thereby highlighting the impact of strong nighttime disturbance winds on the global disturbance dynamo. The nighttime westward winds drive an equatorward current, leading to the accumulation of positive charges at approximately midnight in the low-latitude ionosphere, causing an eastward electric field post-midnight and a westward electric field in the pre-midnight sector.

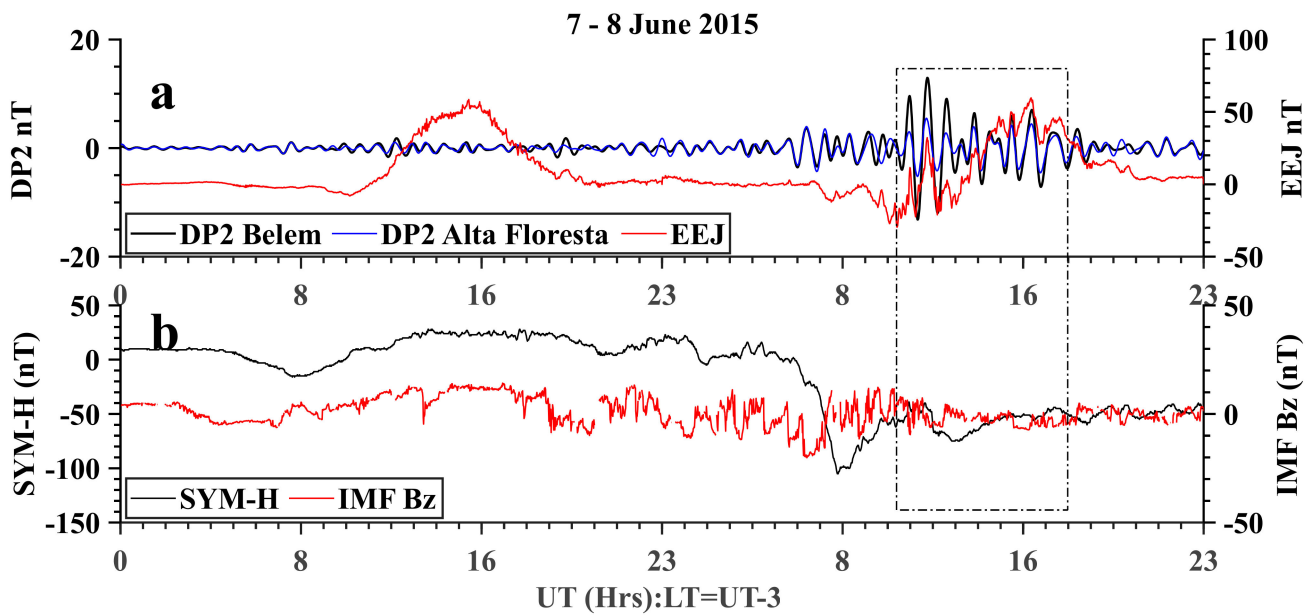


Figure 11. IMF Bz Fluctuations alongside DP2 and EEJ from 7–8 June 2015.

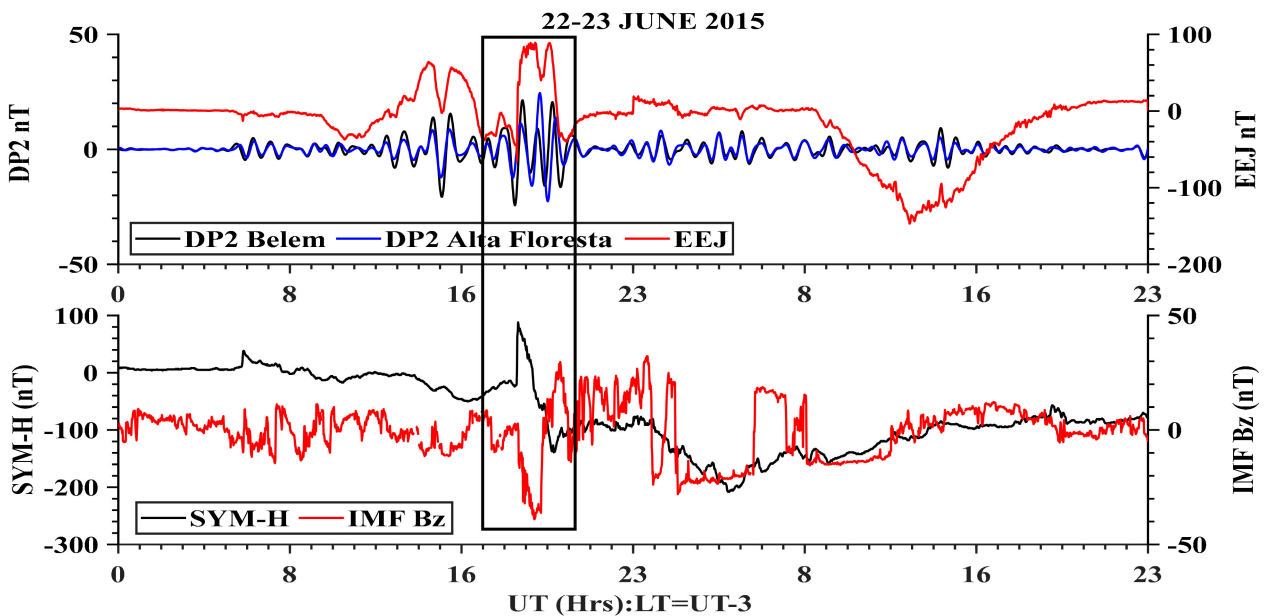


Figure 12. IMF Bz fluctuations alongside the DP2 and EEJ currents from 22 to 23 June 2015.

Figure 4 shows the process of isolating the effect of the disturbance dynamo on the equatorial electric field. The effect of the westward disturbance dynamo can be observed on the EEJ during the day of 23 June 2015 (see Figure 3g). As shown in Panel e of Figure 3,

the recovery phase of the 22–23 June 2015 geomagnetic storms commenced during post-midnight (01:25 LT) on 23 June 2015. Figure 5a shows that the auroral electrojet current intensified during the main phase and early stage of the recovery phase on 23 June. The equatorward storm-time disturbance wind due to Joule heating at the auroral zone can corotate with the Earth to later local times [84,87,88] and drive a large westward disturbance current at low latitudes, as observed in the Brazilian equatorial latitude on 23 June 2015 (see Figure 5b,c). The remarkable amplitude of  $D_{dyn}$  that developed on 23 June can be associated with two distinct factors; (1) The time that the recovery phase commenced on 23 June (01:25 LT) gave the equatorward storm-time wind an ample time to develop and corotate with Earth to dayside superimposing on the background wind and driving large westward ionospheric electric current. (2) The intensification of the auroral electrojet activities at the high latitude which is capable of depositing heat energy into the thermospheric global circulation as we have seen on 22–23 June 2015 in Figures 5a and 6a.

The westward disturbance dynamo caused downward drift of the  $E \times B$  drift velocity on 23 June 2015 (see Figure 7b). The downward drift of the vertical  $E \times B$  drift velocity lowers the ionosphere to the region of high recombination rate and drives negative ionospheric storms, as observed in Figures 7c–l and 8c on 23 June 2015. And, the positive ionospheric storms that characterized the nightside of the main phase and early recovery phase on 23 June can be attributed to the eastward disturbance dynamo electric field [42–44].

In conclusion, we studied the impacts of geomagnetic storms of June 2015 on the Brazilian equatorial and low-latitude ionosphere, and our results showed the following:

- i. The field-aligned currents that originate from dayside reconnections drive the  $DP2$  current system as we have seen in Figures 11 and 12, respectively.
- ii. During the main phase of the 22–23 June geomagnetic storm and in the early stage of the recovery phase, we observed the intensification of auroral activities due to the interaction between the solar wind and the magnetosphere, which caused considerable energy input into the high-latitude auroral ionosphere (see Figures 5a and 6a). The deposition of energy at high latitudes heats the thermosphere, drives equatorward wind surges, and changes global circulation. The change in the global circulation drives downwelling at low latitudes, which decreases molecular species and causes a slight positive ionospheric phase during the main phase on the nightside and early stages of the recovery phase (see Figure 8c). The dynamo effect of the altered wind circulation opposes the normal diurnal variation on 23 June (see Figure 7b), with downward  $E \times B$  drift velocity during the day and drives the negative ionospheric storm during the daytime on 23 June 2015 (see Figures 7c–l and 8c). The westward flow of  $EEJ$  on 23 June was caused by westward disturbance dynamo electric field.
- iii. The interplay between the eastward prompt penetration of magnetospheric electric field and westward disturbance dynamo electric field caused short-lived positive ionospheric storms during the main phase on 22 June 2015 (see Figure 8c)
- iv. The positive ionospheric storm observed during the recovery phase of the 8 June geomagnetic storm was not connected to the eastward prompt penetration of the magnetospheric convection electric field and HSSWs, but the possible driver could be solar flux (F10.7 cm).
- v. A comparison between the *SAMI2 model-VTEC* and *GSP-VTEC* revealed notable disparities in the context of this study. Specifically, the *SAMI2 model* underestimated the VTEC from  $-9^\circ$  to  $-24^\circ$  magnetic latitude in the Brazilian longitudinal sector from 6 to 17 June 2015. However, satisfactory agreement with the *GPS-VTEC* was observed from  $-9^\circ$  to  $10^\circ$  magnetic latitudes from 8 to 15 June 2015. In contrast, the *SAMI2 model* overestimated the VTEC between  $\pm 10^\circ$  magnetic latitudes from 16 to 28 June 2015. The highest root mean square error (RMSE) values, notably 10.30 and 5.48 *TECU*, were recorded on 22 and 23 June 2015, coinciding with periods of intense geomagnetic disturbances. The increase in the RSME value during the main phase on 22 June can be attributed to the interplay between the eastward PPMEF

- and westward DDEF. We recommend that the SAMI2 model should incorporate disturbance winds to optimally perform during intense geomagnetic storms.
- vi. In summary, we observed that the EUVAC model that provides the EUV flux overestimated the ionization during the daytime, particularly from 10:00 to 20:00 LT. These results are not presented to avoid making them cumbersome. Another remarkable observation is that the summer-to-winter hemispheric circulation of meridional neutral wind raised the ionized plasma between  $\pm 10^\circ$  magnetic latitude and lowered it in the Southern Hemisphere, which might be the reason for the overestimation of VTEC by the SAMI2 model between  $\pm 10^\circ$ , as shown in Figures 9 and 10. Finally, we observed that the SAMI2 model failed to reproduce the negative ionospheric storm caused by the westward disturbance dynamo on the VTEC during the daytime on 23 June, as we observed when we compared the SAMI2 model-VTEC on 20 June (quiet day) with that on 23 June (disturbed day). However, when we replaced the Fejer–Scherliess empirical model with the ExB drift velocity estimated from the ground-based magnetometer, the SAMI2 model reproduced the effect of the westward disturbance dynamo on the VTEC on 23 June 2015 (we did not present this result in this study to avoid redundancy) [19]. Hence, we recommend incorporating disturbed winds into the SAMI2 code to achieve optimal performance during geomagnetic storms.

**Author Contributions:** Conceptualization, O.O.A., C.M.N.C. and F.B.-G.; Methodology, O.O.A. and C.A.-M.; Investigation, O.O.A. and C.M.N.C.; Resources, C.A.-M.; Writing—original draft, O.O.A.; Writing—review & editing, F.B.-G. and C.A.-M.; Visualization, O.O.A.; Supervision, C.M.N.C., F.B.-G. and C.A.-M. All authors have read and agreed to the published version of the manuscript.

**Funding:** This research received no external funding.

**Institutional Review Board Statement:** Not applicable.

**Informed Consent Statement:** Not applicable.

**Data Availability Statement:** Data available in a publicly accessible repository that does not issue DOIs. Publicly available datasets were analyzed in this study. This data can be found here: [<https://www.ibge.gov.br>; <http://embracedata.inpe.br>; <http://magnetometers.bc.du>; <https://omniweb.gsfc.nasa.gov> (all of these websites were last accessed on 28 August 2023)].

**Acknowledgments:** We appreciate the Coordination for the Improvement of Higher Education Personnel (CAPES) for the doctoral fellowship through which this research article was implemented. Special thanks go to the Naval Research Laboratory for the open-source SAMI2 model (<https://github.com/sami2py/sami2py>) and Huba for the insightful interaction on the use of the SAMI2 model. We acknowledge Brazilian Network for Continuous Monitoring of the GNSS System (RBMC: <https://www.ibge.gov.br>) for making RINEX GNSS files available, Brazilian study and monitoring of space weather (EMBRAC: <http://embracedata.inpe.br>) and south American Meridional B-Field Array and African Meridian B-Field Education and Research (SAMBA–AMBER: <http://magnetometers.bc.du>) magnetometer data center for making the magnetic data available and OMNIWEB data Center for the interplanetary parameters (<https://omniweb.gsfc.nasa.gov>) (accessed on 10 November 2023).

**Conflicts of Interest:** The authors declare no conflict of interest.

## References

1. Knipp, D.; McQuade, M.K.; Kirkpatrick, D. *Understanding Space Weather and the Physics Behind It*; McGraw-Hill: New York, NY, USA, 2011.
2. Abdu, M.A. Outstanding Problems in the Equatorial Ionosphere-Thermosphere Electrodynamics Relevant to Spread F. *J. Atmos. Sol.-Terr. Phys.* **2001**, *63*, 869–884. Available online: [www.elsevier.nl/locate/jastp](http://www.elsevier.nl/locate/jastp) (accessed on 10 November 2023). [[CrossRef](#)]
3. Greenspan, M.E.; Rasmussen, C.E.; Burke, W.J.; Abdu, M.A. Equatorial density depletions observed at 840 km during the great magnetic storm of March 1989. *J. Geophys. Res. Space Phys.* **1991**, *96*, 13931–13942. [[CrossRef](#)]
4. Balan, N.; Batista, I.S.; Abdu, M.A.; MacDougall, J.; Bailey, G.J. Physical mechanism and statistics of occurrence of an additional layer in the equatorial ionosphere. *J. Geophys. Res. Space Phys.* **1998**, *103*, 29169–29181. [[CrossRef](#)]

5. De Paula, E.R.; de Oliveira, C.B.A.; Caton, R.G.; Negreti, P.M.; Batista, I.S.; Martinon, A.R.F.; Neto, A.C.; Abdu, M.A.; Monico, J.F.G.; Sousasantos, J.; et al. Ionospheric irregularity behavior during the September 6–10, 2017 magnetic storm over Brazilian equatorial–low latitudes. *Earth Planets Space* **2019**, *71*, 42. [[CrossRef](#)]
6. Raghavarao, R.; Wharton, L.E.; Spencer, N.W.; Mayr, H.G.; Brace, L.H. An equatorial temperature and wind anomaly (ETWA). *Geophys. Res. Lett.* **1991**, *18*, 1193–1196. [[CrossRef](#)]
7. Mridula, N.; Pant, T.K. On the possible role of zonal dynamics in the formation and evolution of F3 layers over equator. *J. Atmos. Sol. Terr. Phys.* **2015**, *134*, 69–77. [[CrossRef](#)]
8. Mridula, N.; Pant, T.K.; Manju, G. On the variability of the Equatorial Ionization Anomaly Trough over Indian region: A novel analysis using Beacon TEC measurements. *Adv. Space Res.* **2020**, *66*, 646–654. [[CrossRef](#)]
9. Martinis, C.; Daniell, R.; Eastes, R.; Norrell, J.; Smith, J.; Klenzing, J.; Solomon, S.; Burns, A. Longitudinal Variation of Postsunset Plasma Depletions from the Global-Scale Observations of the Limb and Disk (GOLD) Mission. *J. Geophys. Res. Space Phys.* **2021**, *126*, 028510. [[CrossRef](#)]
10. Cai, X.; Wang, W.; Eastes, R.W.; Qian, L.; Pedatella, N.; Aa, E.; Zhang, S.; Coster, A.; Daniell, R.E.; McClintock, W.E. Equatorial Ionization Anomaly Discontinuity Observed by GOLD, COSMIC-2, and Ground-Based GPS Receivers' Network. *Geophys. Res. Lett.* **2023**, *50*, e2023GL102994. [[CrossRef](#)]
11. Alagbe, G.A.; Afolabi, O.O.; Adagunodo, T.A.; Rabiou, A.B.; Akinwumi, S.A.; Omotosho, T.V. Study of Ionospheric Amplitude Scintillation during Geomagnetic Activities of 2012 at Low Latitude Region. *J. Inform. Math. Sci.* **2017**, *9*, 251–256. Available online: <http://www.rgnpublications.com> (accessed on 26 August 2023).
12. Alagbe, G.A.; Afolabi, O.O.; Fayomi, E.S.; Ayorinde, T.T.; Rabiou, A.B. Latitudinal Variation of Occurrence of Amplitude Scintillations over Lagos and Ilorin. *Int. J. Innov. Res. Adv. Stud. (IJIRAS)* **2017**, *4*. Available online: [www.ijiras.com](http://www.ijiras.com) (accessed on 28 August 2023).
13. Afolabi, O.O.; Adagunodo, T.A.; Akinwumi, S.A.; Usikalu, M.R.; Ayorinde, T.T.; Rabiou, A.B. Impact of magnetic activity on occurrence of ionospheric amplitude scintillation over Lagos, Nigeria. In Proceedings of the 2017 IEEE Radio and Antenna Days of the Indian Ocean, RADIO 2017, Cape Town, South Africa, 25–28 September 2017; Institute of Electrical and Electronics Engineers Inc.: Piscataway, NJ, USA, 2017; pp. 1–2. [[CrossRef](#)]
14. Nishida, A. The origin of fluctuations in the equatorial electrojet; a new type of geomagnetic variation. *Ann. Geophys.* **1966**, *22*, 478.
15. Nishida, A. Geomagnetic DP2 fluctuations and associated magnetospheric phenomena. *J. Geophys. Res.* **1968**, *73*, 1795–1803. [[CrossRef](#)]
16. Nishida, A. Coherence of geomagnetic DP 2 fluctuations with interplanetary magnetic variations. *J. Geophys. Res.* **1968**, *73*, 5549–5559. [[CrossRef](#)]
17. Mayaud, P.N. Comment on 'The Ionospheric Disturbance Dynamo' by M. Blanc and A.D. Richmond. *J. Geophys. Res.* **1982**, *87*, 6353–6355. [[CrossRef](#)]
18. Vasyliunas, V.H. Mathematical model of magnetospheric convection and its coupling to the ionosphere. In *Particles and Fields in the Magnetosphere*; Mc Cormac, B.M., Ed.; D. Reidel Publ. Co.: Dordrecht, The Netherlands, 1970.
19. Tsurutani, B.T.; Verkhoglyadova, O.P.; Mannucci, A.J.; Saito, A.; Araki, T.; Yumoto, K.; Tsuda, T.; Abdu, M.A.; Sobral, J.H.A.; Gonzalez, W.D.; et al. Prompt penetration electric fields (PPEFs) and their ionospheric effects during the great magnetic storm of 30–31 October 2003. *J. Geophys. Res. Space Phys.* **2008**, *113*, 1–10. [[CrossRef](#)]
20. Wolf, R.A. Effects of ionospheric conductivity on convective flow of plasma in the magnetosphere. *J. Geophys. Res.* **1970**, *75*, 4677–4698. [[CrossRef](#)]
21. Spiro, R.W.; Wolf, R.A.; Fejer, B.G. Penetration of high-latitude-electric-field effects to low latitudes during SUNDIAL 1984. *Ann. Geophys.* **1988**, *6*, 39–50.
22. Peymirat, C.; Richmond, A.D.; Koba, A.T. Electrodynamic coupling of high and low latitudes: Simulations of shielding/overshielding effects. *J. Geophys. Res. Space Phys.* **2000**, *105*, 22991–23003. [[CrossRef](#)]
23. Richmond, A.D.; Matsushita, S. Thermospheric response to a magnetic substorm. *J. Geophys. Res.* **1975**, *80*, 2839–2850. [[CrossRef](#)]
24. Blanc, M.; Profile, S.; Richmond, A.D. The Ionospheric Disturbance Dynamo. *J. Geophys. Res. Space Phys.* **1980**, *85*, 1669–1686. Available online: <https://www.researchgate.net/publication/349725008> (accessed on 26 August 2023). [[CrossRef](#)]
25. Fejer, B.G.; De Paula, E.R.; Heelis, R.A.; Hanson, W.B. Hanson Global equatorial ionospheric vertical drifts measured by the AE-E satellite. *J. Geophys. Res.* **1995**, *100*, 5769–5776. [[CrossRef](#)]
26. Fejer, B.G.; Scherliess, L. Empirical models of storm time equatorial zonal electric fields. *J. Geophys. Res. Space Phys.* **1997**, *102*, 24047–24056. [[CrossRef](#)]
27. Kavanagh, L.D.; Freeman, J.W.; Chen, A.J. Plasma flow in the magnetosphere. *J. Geophys. Res.* **1968**, *73*, 5511–5519. [[CrossRef](#)]
28. McPherron, R.L.; Russell, C.T.; Aubry, M.P. Satellite studies of magnetospheric substorms on August 15, 1968: 9. Phenomenological model for substorms. *J. Geophys. Res.* **1973**, *78*, 3131–3149. [[CrossRef](#)]
29. McPherron, R.L. Physical Processes Producing magnetospheric substorms and magnetic storms. *Geomagnetism* **1991**, *4*, 593–739.
30. Strangeway, R.J.; Russell, C.T.; Carlson, C.W.; McFadden, J.P.; Ergun, R.E.; Temerin, M.; Klumpar, D.M.; Peterson, W.K.; Moore, T.E. Cusp field-aligned currents and ion outflows. *J. Geophys. Res. Space Phys.* **2000**, *105*, 21129–21141. [[CrossRef](#)]
31. Wei, Y.; Zhao, B.; Li, G.; Wan, W. Electric field penetration into Earth's ionosphere: A brief review for 2000–2013. *Sci. Bull.* **2015**, *60*, 748–761. [[CrossRef](#)]

32. Ren, Z.; Wan, W.; Wei, Y.; Liu, L.; Yu, T. A theoretical model for mid- and low-latitude ionospheric electric fields in realistic geomagnetic fields. *Sci. Bull.* **2008**, *53*, 3883–3890. [[CrossRef](#)]
33. Knipp, D.J.; Bernstein, V.; Wahl, K.; Hayakawa, H. Timelines as a tool for learning about space weather storms. *J. Space Weather Space Clim.* **2021**, *11*, 29. [[CrossRef](#)]
34. Jaggi, R.K.; Wolf, R.A. Self-consistent calculation of the motion of a sheet of ions in the magnetosphere. *J. Geophys. Res.* **1973**, *78*, 2852–2866. [[CrossRef](#)]
35. Zhang, R.; Liu, L.; Balan, N.; Le, H.; Chen, Y.; Zhao, B. Equatorial Ionospheric Disturbance Field-Aligned Plasma Drifts Observed by C/NOFS. *J. Geophys. Res. Space Phys.* **2018**, *123*, 4192–4201. [[CrossRef](#)]
36. Tsurutani, B. Global dayside ionospheric uplift and enhancement associated with interplanetary electric fields. *J. Geophys. Res.* **2004**, *109*, A08302. [[CrossRef](#)]
37. Tsurutani, B.T.; Lakhina, G.S.; Hajra, R. The physics of space weather/solar-terrestrial physics (STP): What we know now and what the current and future challenges are. *Nonlinear Process. Geophys.* **2020**, *27*, 75–119. [[CrossRef](#)]
38. Tsurutani, B.T.; Gonzalez, W.D.; Tang, F.; Akasofu, S.I.; Smith, E.J. Origin of interplanetary southward magnetic fields responsible for major magnetic storms near solar maximum (1978–1979). *J. Geophys. Res.* **1988**, *93*, 8519. [[CrossRef](#)]
39. Gonzalez, W.D.; Tsurutani, B.T.; Gonzalez, A.L.C.; Smith, E.J.; Tang, F.; Akasofu, S. Solar wind-magnetosphere coupling during intense magnetic storms (1978–1979). *J. Geophys. Res. Space Phys.* **1989**, *94*, 8835–8851. [[CrossRef](#)]
40. Yue, X.; Wan, W.; Liu, L.; Le, H.; Chen, Y.; Yu, T. Development of a middle and low latitude theoretical ionospheric model and an observation system data assimilation experiment. *Chin. Sci. Bull.* **2008**, *53*, 94–101. [[CrossRef](#)]
41. Mazaudier, C. Electric currents above Saint-Santin: 3. A preliminary study of disturbances: June 6, 1978; March 22, 1979; March 23, 1979. *J. Geophys. Res. Space Phys.* **1985**, *90*, 1355–1366. [[CrossRef](#)]
42. Astafyeva, E.; Zakharenkova, I.; Huba, J.D.; Doornbos, E.; Ijssel, J. Global Ionospheric and Thermospheric Effects of the June 2015 Geomagnetic Disturbances: Multi-Instrumental Observations and Modeling. *J. Geophys. Res. Space Phys.* **2017**, *122*, 11–716. [[CrossRef](#)]
43. Astafyeva, E.; Zakharenkova, I.; Hozumi, K.; Alken, P.; Coisson, P.; Hairston, M.R.; Coley, W.R. Study of the Equatorial and Low-Latitude Electrodynamical and Ionospheric Disturbances during the 22–23 June 2015 Geomagnetic Storm Using Ground-Based and Spaceborne Techniques. *J. Geophys. Res. Space Phys.* **2018**, *123*, 2424–2440. [[CrossRef](#)]
44. Singh, R.; Sripathi, S. Ionospheric Response to 22–23 June 2015 Storm as Investigated Using Ground-Based Ionosondes and GPS Receivers Over India. *J. Geophys. Res. Space Phys.* **2017**, *122*, 11645–11664. [[CrossRef](#)]
45. Macho, E.P.; Correia, E.; Paulo, C.M.; Angulo, L.; Vieira, J.A.G. Ionospheric response to the June 2015 geomagnetic storm in the South American region. *Adv. Space Res.* **2020**, *65*, 2172–2183. [[CrossRef](#)]
46. Paul, B.; De, B.K.; Guha, A. Latitudinal variation of F-region ionospheric response during three strongest geomagnetic storms of 2015. *Acta Geod. Et Geophys.* **2018**, *53*, 579–606. [[CrossRef](#)]
47. Mansilla, G.A. Ionospheric Response to the Magnetic Storm of 22 June 2015. *Pure Appl. Geophys.* **2018**, *175*, 1139–1153. [[CrossRef](#)]
48. Amaechi, P.O.; Oyeyemi, E.O.; Akala, A.O. Geomagnetic storm effects on the occurrences of ionospheric irregularities over the African equatorial/low-latitude region. *Adv. Space Res.* **2018**, *61*, 2074–2090. [[CrossRef](#)]
49. Gopi. GPS-TEC Analysis Software. 2011. Available online: <https://www.researchgate.net/publication/255978205> (accessed on 26 August 2023).
50. Rastogi, R.G.; Kitamura, T.; Kitamura, K. Geomagnetic field variations at the equatorial electrojet station in Sri Lanka, Peredinia. *Ann. Geophys.* **2004**, *22*, 2729–2739. [[CrossRef](#)]
51. Agodi Onwumechili, C. *The Equatorial Electrojet*; Overseas Publishers Association, Amsterdam B.V. Published in the Netherlands under license by Gordon and Breach Science Publishers: Amsterdam, The Netherlands, 1997.
52. Rabiou, A.B.; Folarin, O.O.; Uozumi, T.; Abdul Hamid, N.S.; Yoshikawa, A. Longitudinal variation of equatorial electrojet and the occurrence of its counter electrojet. *Ann. Geophys.* **2017**, *35*, 535–545. [[CrossRef](#)]
53. Amaechi, P.O.; Oyeyemi, E.O.; Akala, A.O.; Messanga, H.E.; Panda, S.K.; Seemala, G.K.; Oyedokun, J.O.; Fleury, R.; Amory-Mazaudier, C. Ground-Based GNSS and C/NOFS Observations of Ionospheric Irregularities Over Africa: A Case Study of the 2013 St. Patrick's Day Geomagnetic Storm. *Space Weather* **2021**, *19*, e2020SW002631. [[CrossRef](#)]
54. Younas, W.; Amory-Mazaudier, C.; Khan, M.; Le Huy, M. Magnetic Signatures of Ionospheric Disturbance Dynamo for CME and HSSWs Generated Storms. *Space Weather* **2021**, *19*, e2021SW002825. [[CrossRef](#)]
55. Mene, N.M.; Koba, A.T.; Obrou, O.K.; Zaka, K.Z.; Boka, K.; Amory-Mazaudier, C.; Assamoi, P. Statistical study of the DP2 enhancement at the dayside dip-equator compared to low latitudes. *Ann. Geophys.* **2011**, *29*, 2225–2233. [[CrossRef](#)]
56. Amory-Mazaudier, C.; Bolaji, O.S.; Doumbia, V. On the historical origins of the CEJ, DP2, and Ddyn current systems and their roles in the predictions of ionospheric responses to geomagnetic storms at equatorial latitudes. *J. Geophys. Res. Space Phys.* **2017**, *122*, 7827–7833. [[CrossRef](#)]
57. Younas, W.; Amory-Mazaudier, C.; Khan, M.; Fleury, R. Ionospheric and Magnetic Signatures of a Space Weather Event on 25–29 August 2018: CME and HSSWs. *J. Geophys. Res. Space Phys.* **2020**, *125*, e2020JA027981. [[CrossRef](#)]
58. Rodríguez-Zuluaga, J.; Radicella, S.M.; Nava, B.; Amory-Mazaudier, C.; Mora-Páez, H.; Alazo-Cuartas, K. Distinct responses of the low-latitude ionosphere to CME and HSSWS: The role of the IMF Bz oscillation frequency. *J. Geophys. Res. Space Phys.* **2016**, *121*, 11528–11548. [[CrossRef](#)]

59. Le Huy, M. Magnetic signature of the ionospheric disturbance dynamo at equatorial latitudes: ‘ $D_{\text{dyn}}$ ’. *J. Geophys. Res.* **2005**, *110*, A10301. [CrossRef]
60. Nava, B.; Rodríguez-Zuluaga, J.; Alazo-Cuartas, K.; Kashcheyev, A.; Migoya-Orué, Y.; Radicella, S.; Amory-Mazaudier, C.; Fleury, R. Middle- and low-latitude ionosphere response to 2015 St. Patrick’s Day geomagnetic storm. *J. Geophys. Res. A Space Phys.* **2016**, *121*, 3421–3438. [CrossRef]
61. Huang, N.E.; Shen, Z.; Long, S.R.; Wu, M.C.; Shih, H.H.; Zheng, Q.; Yen, N.-C.; Tung, C.C.; Liu, H.H. The empirical mode decomposition and the Hilbert spectrum for nonlinear and non-stationary time series analysis. *Proc. R. Soc. Lond. Ser. A Math. Phys. Eng. Sci.* **1998**, *454*, 903–995. [CrossRef]
62. Flandrin, P.; Rilling, G.; Goncalves, P. Empirical Mode Decomposition as a Filter Bank. *IEEE Signal Process. Lett.* **2004**, *11*, 112–114. [CrossRef]
63. Dragomiretskiy, K.; Zosso, D. Variational Mode Decomposition. *IEEE Trans. Signal Process.* **2014**, *62*, 531–544. [CrossRef]
64. Cooper, G.R.J.; Cowan, D.R. Comparing time series using wavelet-based semblance analysis. *Comput. Geosci.* **2008**, *34*, 95–102. [CrossRef]
65. Torrence, C.; Compo, G.P. A Practical Guide to Wavelet Analysis. *Bull. Am. Meteorol. Soc.* **1998**, *79*, 61–78. [CrossRef]
66. Cowley, S.W.H. The Earth’s magnetosphere: A brief beginner’s guide. *Eos Trans. Am. Geophys. Union* **1995**, *76*, 525. [CrossRef]
67. Akasofu, S.-I. Energy coupling between the solar wind and the magnetosphere. *Space Sci. Rev.* **1981**, *28*, 121–190. [CrossRef]
68. Huba, J.D.; Joyce, G.; Fedder, J.A. Sami2 is Another Model of the Ionosphere (SAMI2): A new low-latitude ionosphere model. *J. Geophys. Res. Space Phys.* **2000**, *105*, 23035–23053. [CrossRef]
69. Huba, J.D.; Joyce, G.; Fedder, J.A. The formation of an electron hole in the topside equatorial ionosphere. *Geophys. Res. Lett.* **2000**, *27*, 181–184. [CrossRef]
70. Richards, P.G.; Fennelly, J.A.; Torr, D.G. EUVAC: A solar EUV flux model for aeronomic calculations. *J. Geophys. Res.* **1994**, *99*, 8981. [CrossRef]
71. Iyemori, T.; Rao, D.R.K. Decay of the Dst field of geomagnetic disturbance after substorm onset and its implication to storm-substorm relation. *Ann. Geophys.* **1996**, *14*, 608–618. [CrossRef]
72. Grocott, A.; Milan, S.E.; Baker, J.B.H.; Freeman, M.P.; Lester, M.; Yeoman, T.K. Dynamic subauroral ionospheric electric fields observed by the Falkland Islands radar during the course of a geomagnetic storm. *J. Geophys. Res. Space Phys.* **2011**, *116*, A11202. [CrossRef]
73. Piersanti, M.; Alberti, T.; Bemporad, A.; Berrilli, F.; Bruno, R.; Capparelli, V.; Carbone, V.; Cesaroni, C.; Consolini, G.; Cristaldi, A.; et al. Comprehensive Analysis of the Geoeffective Solar Event of 21 June 2015: Effects on the Magnetosphere, Plasmasphere, and Ionosphere Systems. *Sol. Phys.* **2017**, *292*, 169. [CrossRef]
74. Fathy, I.; Amory-Mazaudier, C.; Fathy, A.; Mahrous, A.M.; Yumoto, K.; Ghamry, E. Ionospheric disturbance dynamo associated to a coronal hole: Case study of 5–10 April 2010. *J. Geophys. Res. Space Phys.* **2014**, *119*, 4120–4133. [CrossRef]
75. Fuller-Rowell, T.J.; Codrescu, M.V.; Moffett, R.J.; Quegan, S. Response of the thermosphere and ionosphere to geomagnetic storms. *J. Geophys. Res.* **1994**, *99*, 3893. [CrossRef]
76. Fuller-Rowell, T.J.; Codrescu, M.V.; Roble, R.G.; Richmond, A.D. How Does the Thermosphere and Ionosphere React to a Geomagnetic Storm? American Geophysical Union: Washington, DC, USA, 1997; pp. 203–225. [CrossRef]
77. Fuller-Rowell, T.J.; Codrescu, M.V.; Rishbeth, H.; Moffett, R.J.; Quegan, S. On the seasonal response of the thermosphere and ionosphere to geomagnetic storms. *J. Geophys. Res. Space Phys.* **1996**, *101*, 2343–2353. [CrossRef]
78. Baker, W.G.; Martyn, D.F. Electric Currents in the Ionosphere I. The Conductivity. *Philos. Trans. R. Soc. Lond. Ser. A Math. Phys. Sci.* **1953**, *246*, 281–294. Available online: <https://royalsocietypublishing.org/> (accessed on 10 November 2023).
79. Zhang, R.; Liu, L.; Le, H.; Chen, Y.; Kuai, J. The Storm Time Evolution of the Ionospheric Disturbance Plasma Drifts. *J. Geophys. Res. Space Phys.* **2017**, *122*, 11665–11676. [CrossRef]
80. Yizengaw, E.; Moldwin, M.B.; Zesta, E.; Magoun, M.; Pradipta, R.; Biouele, C.M.; Rabiou, A.B.; Obrou, O.K.; Bamba, Z.; de Paula, E.R. Response of the equatorial ionosphere to the geomagnetic DP2 current system. *Geophys. Res. Lett.* **2016**, *43*, 7364–7372. [CrossRef]
81. Clauer, C.R.; Kamide, Y. DP 1 and DP 2 current systems for the March 22, 1979 substorms. *J. Geophys. Res. Space Phys.* **1985**, *90*, 343–1354. [CrossRef]
82. Kikuchi, T.; Lühr, H.; Schlegel, K.; Tachihara, H.; Shinohara, M.; Kitamura, T.-I. Penetration of auroral electric fields to the equator during a substorm. *J. Geophys. Res. Space Phys.* **2000**, *105*, 23251–23261. [CrossRef]
83. Kikuchi, T.; Lühr, H.; Kitamura, T.; Saka, O.; Schlegel, K. Direct penetration of the polar electric field to the equator during a DP 2 event as detected by the auroral and equatorial magnetometer chains and the EISCAT radar. *J. Geophys. Res. Space Phys.* **1996**, *101*, 17161–17173. [CrossRef]
84. Xiong, C.; Lühr, H.; Fejer, B.G. The response of equatorial electrojet, vertical plasma drift, and thermospheric zonal wind to enhanced solar wind input. *J. Geophys. Res. Space Phys.* **2016**, *121*, 5653–5663. [CrossRef]
85. Fejer, B.G.; Scherliess, L. Time dependent response of equatorial ionospheric electric fields to magnetospheric disturbances. *Geophys. Res. Lett.* **1995**, *22*, 851–854. [CrossRef]
86. Richmond, A.D.; Peymirat, C.; Roble, R.G. Long-lasting disturbances in the equatorial ionospheric electric field simulated with a coupled magnetosphere-ionosphere-thermosphere model. *J. Geophys. Res. Space Phys.* **2003**, *108*, 1118. [CrossRef]

- 
87. Fuller-Rowell, T.J.; Millward, G.H.; Richmond, A.D.; Codrescu, M.V. Storm-time changes in the upper atmosphere at low latitudes. *J. Atmos. Sol. Terr. Phys.* **2002**, *64*, 1383–1391. [[CrossRef](#)]
  88. Emmert, J.T.; Fejer, B.G.; Shepherd, G.G.; Solheim, B.H. Average nighttime *F* region disturbance neutral winds measured by UARS WINDII: Initial results. *Geophys. Res. Lett.* **2004**, *31*, L22807. [[CrossRef](#)]

**Disclaimer/Publisher’s Note:** The statements, opinions and data contained in all publications are solely those of the individual author(s) and contributor(s) and not of MDPI and/or the editor(s). MDPI and/or the editor(s) disclaim responsibility for any injury to people or property resulting from any ideas, methods, instructions or products referred to in the content.